Delft University of Technology

Modeling the chloride transport in concrete from microstructure generation to chloride diffusivity prediction

Tong, Liang yu; Liu, Qing feng; Xiong, Qingxiang; Meng, Zhaozheng; Amiri, Ouali; Zhang, Mingzhong

Important note
To cite this publication, please use the final published version (if applicable).
Please check the document version above.

RESEARCH ARTICLE

COMPUTER-AIDED CIVIL AND INFRASTRUCTURE ENGINEERING   WILEY

Modeling the chloride transport in concrete from microstructure generation to chloride diffusivity prediction

Liang-yu Tong[1] | Qing-feng Liu[1,2] | Qingxiang Xiong[1] | Zhaozheng Meng[1,3] | Ouali Amiri[4] | Mingzhong Zhang[5]

[1]State Key Laboratory of Ocean Engineering, School of Ocean and Civil Engineering, Shanghai Jiao Tong University, Shanghai, China

[2]Chongqing Research Institute, Shanghai Jiao Tong University, Chongqing, China

[3]Microlab, Faculty of Civil Engineering and Geosciences, Delft University of Technology, Delft, The Netherlands

[4]GeM, Research Institute of Civil Engineering and Mechanics, Université de Nantes, , UMR CNRS, Nantes, France

[5]Department of Civil, Environmental and Geomatic Engineering, University College London, London, UK

Correspondence
Qing-feng Liu, School of Ocean and Civil Engineering, Shanghai Jiao Tong University, Shanghai, China.
Email: liuqf@sjtu.edu.cn

Zhaozheng Meng, Faculty of Civil Engineering and Geosciences, Delft University of Technology, Delft, The Netherlands.
Email: z.meng@tudelft.nl

Abstract

Pore structure characteristics of cementitious materials play a critical role in the transport properties of concrete structures. This paper develops a novel framework for modeling chloride penetration in concrete, considering the pore structure-dependent model parameters. In the framework, a multi-scale transport model was derived by linking the chloride diffusivities with pore size distributions (PSDs). Based on the three-dimensional (3D) microstructure generated by "porous growth" and "hard core-soft shell" methods, two sub-models were computationally developed for determining the multi-modal PSDs and pore size-related chloride diffusivities. The predicted results by these series of models were compared with corresponding experimental data. The results indicated that by adopting pore size-related diffusivities, even if the total porosities were the same, the proposed multi-scale chloride transport model could better capture the effect of different PSDs on chloride penetration profiles, while the model without pore structure-depended parameters would ignore the differences. Compared with the reference transport models, which adopt averaged chloride diffusivities, the chloride penetration depths predicted by the proposed multi-scale model are in better agreement with experimental data, with 10%–25% reduced prediction error. This multi-scale transport model is hoped to provide a novel computational approach on 3D microstructure generation and better reveal the underlying mechanism of the chloride penetration process in concrete from a microscopic perspective.

1 | INTRODUCTION

Chloride-induced corrosion is thought to be one of the major deteriorations in reinforced concrete (RC) structures served in different environments (Q.-F. Liu, 2022), such as marine environments (Sakai, 2019), transport systems (Shi et al., 2009), and infrastructure elements (Kliukas et al., 2018). Once the chloride concentration around the reinforcing steel reaches a threshold value, de-passivation of the reinforcement will occur and lead to mechanical strength loss (X. Li et al., 2024). Thus, the penetration of chloride ions into concrete cover is generally regarded as the initial stage of chloride-induced damage and remains a hot topic related to structural durability (Meng et al., 2022; Q.-F. Liu et al., 2023). Apparently, the chloride penetration in concrete is highly influenced by the microscopic characteristics, such as total porosity and pore size distribution (PSD; Y. Guo et al., 2021; Provis et al., 2012). These pore structure features are strongly associated with many factors such as water-to-cement ratio (*w/c*), curing conditions and curing times. As the hydration proceeds, the pore structure of concrete will be denser, more tortuous, and less connected with reduced porosity, which can alleviate chloride penetration and thus enhance concrete durability. Therefore, for cementitious materials, adequate predictions of chloride penetration and assessment of the durability of RC structures should take into account the pore structure of cementitious materials of different sizes, including both gel and capillary pores (Gan, Romero Rodriguez, Zhang, et al., 2021).

At present, several experimental works have been presented to explore the mechanism of chloride-induced corrosion in RC concrete from pore-scale viewpoints (Gan, Romero Rodriguez, Schlangen, et al., 2021; Provis et al., 2012). Different practical techniques, such as electrical conductivity experiments and mercury intrusion porosimetry (MIP), were implemented to determine the pore structure of concrete. Through fitting the tested data of microscopic features (e.g., porosity) and ionic diffusivities, which can generally be measured by the natural immersion method and accelerated chloride diffusion tests (Tong et al., 2021), several theoretical equations and some types of empirical models have been proposed (Hu et al., 2019; Xiong & Meftah, 2021). For instance, Y. Zhang and Ye (2019) proposed an empirical equation to analyze the relationship between the ionic diffusion coefficient at different saturation degrees and the peak pore radiuses of PSD curves obtained from MIP. However, the experiments are usually time-consuming and costly (Rafiei et al., 2017a); the samples used to test the pore structure characteristics may afford some damage during testing procedures (e.g., cracking may appear in MIP tests; Y. Zhang et al., 2020), leading to unexpected errors in final results. Furthermore,

despite the simplicity of the proposed empirical equations, certain conditions are desired when using these equations. The underlying mechanisms of chloride penetration in concrete with complex pore structures need further study (Ahmadkhanlou & Adeli, 2005).

Except for experimental works, several numerical works have also been carried out (Hafezolghorani et al., 2022; Rafiei et al., 2016). The first type of pore structure-related model is proposed based on mass conservation law, the Nernst–Planck equation or Fick's law (B. Guo et al., 2018). To relate the ionic transport properties with the microscopic properties of concrete, Dingshi Chen et al. (2021) introduced empirical equations to consider the impact of microscopic parameters on the electrostatic migration and chloride binding. The first type of model is usually computationally efficient. However, due to the limitation of empirical equations that reflect complex pore structures with simple one or two parameters illustrated above, these models ignore the effect of widely ranged pore sizes, from nano-gel pores to micro-capillary pores, on the transport properties of concrete. In contrast, McDonald et al. (2010) and Huang et al. (2015) experimentally reported that gel pores play a significant role in ionic diffusion and should be carefully considered during transport modeling. To tackle the limitation of this kind of macro-model, the second type of model, the pure pore-scale model, was proposed to directly capture the pore structure features on effective transport properties of concrete (Blunt et al., 2013). In these studies, based on the two-dimensional (2D) and three-dimensional (3D) generated microstructure of cementitious materials, the chloride diffusivity is predicted by adopting analytical homogenization methods (Tong et al., 2023; Xiong et al., 2023), finite element method (Q.-F. Liu et al., 2023) and lattice Boltzmann method (Rafiei et al., 2017b). Through these, the pore structure's effect can be directly considered in chloride diffusivity predictions and thus seem more accurate than macro-models, which combine with empirical equations (Bernard et al., 2003; Q.-F. Liu et al., 2022). But during the modeling, the simulations of chloride transport by pure-scale modeling are still time-consuming (Bishnoi & Scrivener, 2009; Zheng et al., 2019). Nevertheless, pure pore-scale studies are always limited to small-size representative volume elements (RVEs) rather than concrete (Adeli & Kim, 2001).

For large-size concrete structures, multi-scale models were used to consider the features of concrete from micro- to macro-features (Tong et al., 2023). At the macro-scale, concrete is generally viewed as a homogenous block (Cai et al., 2022). At the meso-scale, concrete is treated as the three-phase assemblage of cement paste, interface transition zones (ITZs), and aggregates (Aldwaik & Adeli, 2016; Wan et al., 2024). At the micro-scale, the volume fraction, location and orientation of different hydration

products, pores, and anhydrous clinkers in cement paste can be visually presented in RVEs. Although hetergeneous features of different scales can be considered in the multi-scale models, however, most existing multi-scale models still adopted analytical or numerical homogenization approaches to deliver parameters between different scales, which may wear out the pore structure features of lower scales (Meng, Liu, et al., 2024). Thus, it is vital to develop a multi-scale model that is useful in predicting the ions transport process at the concrete scale and able to capture the "real" pore structure containing widely ranged pore sizes and analyze their impact on chloride transport from micro- to macro-scale thoroughly.

This work aims to propose a numerical framework to investigate the chloride penetration in concrete accounting for the thorough effects of ITZs, aggregates, gel, and small and large capillary pores (LCPs). A multi-scale chloride transport model will be derived considering multi-modal PSDs $p(r)$ and pore size-related diffusivity $D(r)$. Considering different factors, including chemical composition, w/c ratio, and hydration degree, the voxel-based microstructures of cement paste will be generated in the framework using novelly proposed "porous growth" and "hard core-soft" shell methods to better reveal the connectivity of pore structure. Based on the generated microstructure, $p(r)$ and $D(r)$ will be obtained, respectively, from two sub-models, that is, a PSD model that can extract the multi-modal PSDs covering different ranges of pores and a lattice diffusion model that can predict the chloride diffusivity at the steady state. The predicted results of the sub-models and multi-scale transport models are compared with third-party experimental data, and the results are predicted by models that do not fully consider the widely ranged pore sizes. The proposed modeling framework is going to improve the prediction accuracy of chloride penetration depth in concrete and better capture the effect of different pore size groups on transport properties.

2 | MULTI-SCALE CHLORIDE TRANSPORT MODEL

The present study is going to propose a multi-scale model to directly capture the intrinsic effects of different pore sizes on the macro-scale chloride penetration process. Thus, concrete in a saturated isothermal state is considered, in which chloride penetration is generally driven by the concentration gradient and electrostatic potential. To model the transport process, it can be described as (Meng, Zhang, et al., 2024; Qiu & Dai, 2021):

$$\frac{\partial C}{\partial t} = D_c \nabla^2 C + D_c \frac{FZ}{RT} \nabla (C \nabla \Phi) \quad (1)$$

where C and D_c is the concentration (mol/m^3) and diffusion coefficient (m^2/s) of chloride ions in concrete, respectively; Z is the ionic charge number, which is valued at -1 for chloride; R (8.314 J/mol/K) is the ideal gas constant; T (298.15K) is the absolute temperature; F is the Faraday constant (9.648 ×10^{4}C/mol), and Φ presents the electrostatic potential (V).

At the meso-scale, the chloride diffusion coefficient in the saturated isothermal state could also be influenced by the chloride binding, the presence of aggregates, and ITZs (De Chen et al., 2024; Patel et al., 2021). Considering these influences, the chloride diffusion coefficient D_c in Equation (1) should be:

$$D_c = f_B \cdot f_A \cdot f_{ITZ} \cdot D \quad (2)$$

in which D (m^2/s) presents the chloride diffusion coefficient of the cement paste; parameters f_B, f_A, f_{ITZ} indicates the effect of chloride binding, presence of aggregates, and ITZs and can be determined as follows:

(1) Influence of chloride binding: f_B. To determine the concentration of bound and free chloride ions, three kinds of binding isotherms are generally adopted: linear, Langmuir, and Freundlich isotherms (Luping & Nilsson, 1993a). Several studies have certified that the linear isotherm is oversimplified and could misestimate the bound chloride's concentration (Martín-Pérez et al., 2000). Therefore, the Langmuir and Freundlich isotherms are adopted in the present study. According to Dingshi Chen et al. (2021), the impact factor f_B can be determined as

$$f_B = \frac{1}{1+B}, \quad B = \begin{cases} \frac{\alpha}{(1+\beta C)^2} & C \le 50\text{mol/m}^3 \\ \alpha'\beta'C^{\beta'-1} & C > 50\text{mol/m}^3 \end{cases} \quad (3)$$

where B is the value for the assessment of the chloride binding capacity, α, β, α', and β' are the adsorption isotherm parameters according to Martín-Pérez et al. (2000).

(2) Influence of aggregates: f_A. The presence of aggregates can elongate the lengths traveled by chloride ions (Jin et al., 2023). Based on the effect of sands or aggregates, the predicted chloride diffusion coefficient has to be multiplied by a reduction factor considering the tortuosity effect of sand and aggregate. To determine the reduction, several relationships have been proposed in the literature. In this study, the equation proposed by
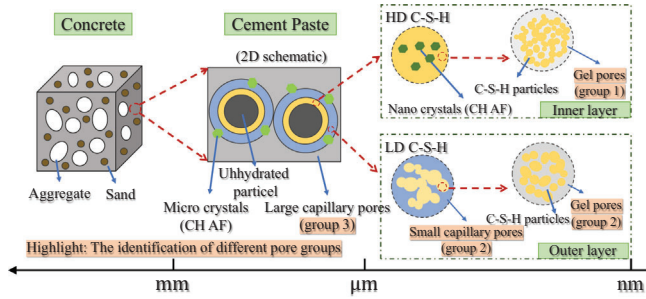
FIGURE 1 Representative volume elements (RVEs) of concrete and cement paste.

FIGURE 2 Schematic description of individual and overall multi-modal pore size distributions (PSDs).

Chidiac and Shafikhani (2019) is used as Equation (4).

$$f_A = \frac{3(1 - V_a)^2}{3 - V_a} \tag{4}$$

where V_a is the aggregates' volume fraction.

(3) Influence of ITZs: f_{ITZ}. ITZs are around the aggregate particles, which have higher porosity and diffusivity than the bulk cement paste (Dridi, 2012). The derived equation by Shafikhani and Chidiac (2020) is adopted here to present the effect of ITZs on ionic diffusivity:

$$f_{ITZ} = \frac{12 + 18V_{ITZ}}{12 - 9V_{ITZ}} \tag{5}$$

where V_{ITZ} is the ITZs' volume fraction and can be determined based on the particle size distribution of mixed aggregates. The calculation procedure can be found in the author's previous study (Tong et al., 2023).

At the pore-scale (micro-scale), compared with cement paste, which contains pore networks, aggregates and sands can be treated as impermeable composites during chloride transport. Thus, an idealized small volume of cement paste in concrete is selected as RVE to analyze the microstructural features and transport channels. As the 2D schematic displayed in Figure 1, cement paste can be modeled as an assemblage of micro-size crystal hydrates and calcium silicate hydrate (C-S-H), which are generated at the surface of anhydrous cement particles and LCPs ($100\ nm < d < 1000\ nm$; Achour et al., 2020; Bernard et al., 2003). More precisely, due to different densities, two layers of C-S-H gels can be classified as: an outer layer consisting of low-density C-S-H (LD C-S-H) and small capillary pores (SCPs, $10\ nm < d < 100\ nm$); an inner layer composed of high-density C-S-H (HD C-S-H) and nano-crystals. Besides, the LD and HD C-S-H can be regarded as a mixture of gel pores ($d < 10\ nm$) and solid C-S-H particles (Achour et al., 2020; Tennis & Jennings, 2000).
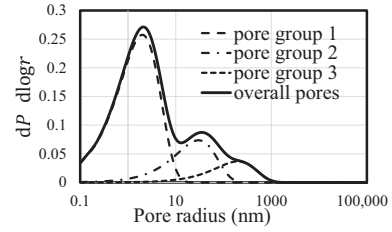
Based on the pores' location and their sizes illustrated above, the PSD for typical hardened cement paste, which owns an extensive range of pore sizes, from nano- to micro-scales, could be divided into three groups as highlighted in Figure 1: pores in inner layer (pore group 1), pores in outer layer (pore group 2), and LCPs (pore group 3). If defining the PSD function as $p(r)$, three components of pore groups in cement paste should be considered together here in $p(r)$ and be expressed as a multi-modal PSD:

$$p(r) = \sum_{i=1}^{3} \gamma_i p_i(r) \text{ with } \int_{r_{min}}^{r_{max}} p(r)\,dr = 1 \text{ and } \int_{r_{min}}^{r_{max}} p_i(r)\,dr = 1 \tag{6}$$

where i can be group 1, 2, and 3; $\gamma_i = \frac{\rho_i}{\rho}$ are porosity proportions of different pore groups, ρ means total porosity, and ρ_i present porosity of each pore group; r_{min} and r_{max} are considered pore size lower and upper limits, respectively; in the present study, the pore size range $[r_{min}, r_{max}]$ is set as [0.1, 10,000 nm] (Huang et al., 2015). It was reported that the pore size obeys a statistical behavior and can be described by the probabilistic models such as Rayleigh–Ritz (R-R) distribution (Maekawa et al., 2003), normal distribution (Lu et al., 2002), and lognormal distribution (Xiong et al., 2024).

In the present study, each pore group is assumed to follow the R-R model. Thus, the cumulative PSD function $P(r)$ and PSD $p(r)$ are a sum of three pore groups and can be expressed by a multiple R-R model:

$$P(r) = \sum_{i=1}^{3} \gamma_i P_i(r) = \sum_{i=1}^{3} \gamma_i \left(1 - \exp\left(-\frac{r}{B_i}\right)\right) \tag{7}$$

$$p(r) = \frac{dP(r)}{d\log(r)} = \sum_{i=1}^{3} r \frac{\gamma_i}{B_i} \exp\left(-\frac{r}{B_i}\right) d\log(r) \tag{8}$$

where B_i are the peak pore radius for groups 1, 2, and 3 (nm), which correspond to the peak on a logarithmic scale; With different B_i, different pore groups can have different pore size proportions through the pore size range $[r_{min}, r_{max}]$ as illustrated in Figure 2.
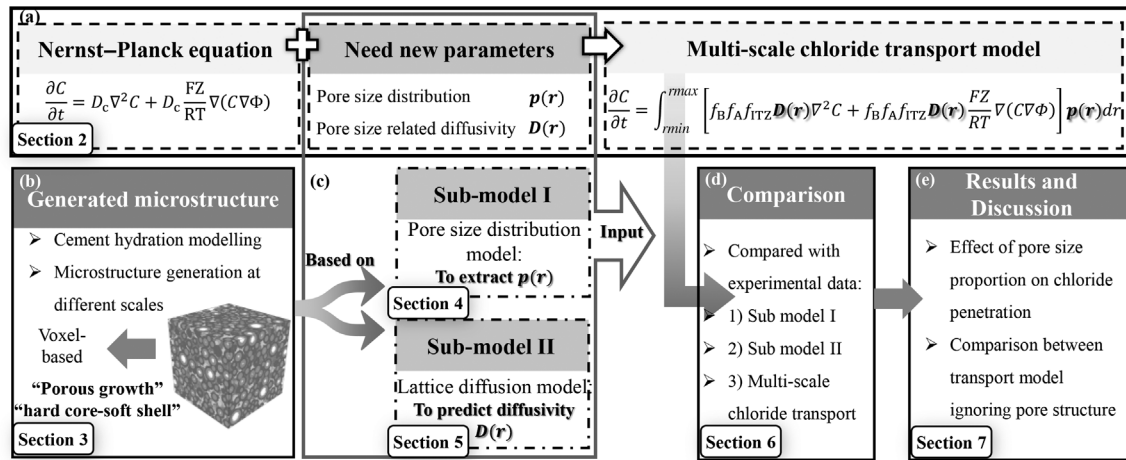
FIGURE 3 Outline of the present study. (a) Development of multi-scale chloride transport model, (b) microstructure generation, (c) description of Sub-models I and II, (d) comparison of modeled and experimental results, and (e) results and discussion.

In Equation (1), the diffusion coefficient (D) was adopted to homogenize the whole pore structure, which treats cementitious materials as a homogeneous block, disregarding different pore groups of concrete. However, cement paste is a heterogeneous component at the microscale. Therefore, using D to predict the transport process may underestimate the chloride transport within large pore channels, leading to a smaller penetration depth. Similarly, it may overestimate the chloride transport in small pore channels, resulting in a larger penetration depth. Therefore, to improve the prediction accuracy of chloride penetration depth, the commonly used chloride diffusion coefficient D should be transformed to a pore size-related $D(r)$. Combing the multi-modal PSDs $p(r)$ and chloride diffusivity D, the pore size-related diffusivity $D(r)$ can be expressed as Equation (9) to thoroughly investigate the effect of widely ranged pore structure on chloride penetration:

$$D = \int_{r_{\min}}^{r_{\max}} D(r) p(r) dr = \sum_{i=1}^{3} \gamma_i \int_{r_{\min}}^{r_{\max}} D(r) p_i(r) dr \quad (9)$$

So, considering ITZs, aggregates, and different pore sizes, a multi-scale chloride transport model can be proposed. Bringing Equations (2) and (9) into Equation (1), the governing equation for the chloride penetration process can be described as follows:

$$\frac{\partial C}{\partial t} = \int_{r_{\min}}^{r_{\max}} \left[f_B \cdot f_A \cdot f_{ITZ} \cdot D(r) \nabla^2 C \right.$$
$$\left. + f_B \cdot f_A \cdot f_{ITZ} \cdot D(r) \frac{FZ}{RT} \nabla (C \nabla \Phi) \right] p(r) dr \quad (10)$$

The outline of the present study is described in Figure 3. In this study, Section 2 develops a multi-scale chloride

transport model to explore the influence of microscopic characteristics on chloride penetration in concrete as shown in Figure 3a. Through this novel governing equation, the effect of PSD on the chloride penetration process can be directly captured. Therefore, in the present study, obtaining pore size-related chloride diffusivity $D(r)$ and the distribution function $p(r)$ is vital for solving the governing equation. Considering that both PSD and chloride diffusivity are closely related to the geometrical morphologies of cement paste, multi-scale microstructures will first be generated through the "porous growth" and "hard core-soft shell" method in Section 3 as shown in Figure 3b. Based on the generated microstructure, the first sub-model: the PSD model for extraction of multi-modal PSDs, and the second sub-model: lattice diffusion model for the chloride diffusivity prediction in concrete, will be described in detail in Sections 4 and 5, respectively, as listed in Figure 3c. Subsequently, Section 6 will compare the modeled results of Sub-models I, II, and the multi-scale chloride transport model with experimental data, see Figure 3d. Then, a detailed analysis of the influence of different pore groups on the penetration process will be given in Section 7 as shown in Figure 3e. Finally, a conclusion of the text will be provided.

3 | GENERATION OF VOXEL-BASED MICROSTRUCTURE

Various computer-aided technologies have been proposed in the past decades to simulate the 3D microstructure of cement paste. Among them, several helpful software are widely used, for example, CEMHYD3D (Bentz, 1997), HYMOSTRUC3D (Ye et al., 2003), and μic (Bishnoi & Scrivener, 2009). In the present study, Section 2 has illustrated that a whole range of pore sizes is needed for the
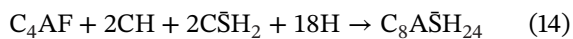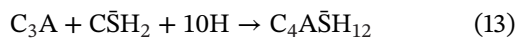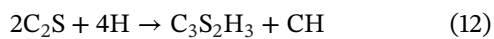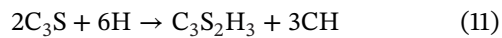
proposed multi-scale transport model. However, limited by the resolution of a single-scale digitized microstructure obtained by the existing software (generally 0.1~1 μm/voxel), a range of length scale of pores, including parts of capillary pores and nano-sized gel pores, cannot be fully covered (M. Zhang et al., 2012). Considering that heterogeneous pore structure in cement paste owns an extensive range of pore sizes, from nano- to micro-scales, RVEs will be generated by a voxel-based method at multi-scales in the present section.

Herein, considering cement chemical composition, w/c ratio, curing temperatures, and curing ages, the cement hydration process will be analytically analyzed. The calculation procedures for each composite's volume fraction will be illustrated in Section 3.1. Based on the calculated volume fraction, the multi-scale microstructures of cement paste, which will be used in the subsequent two sub-models, will be generated using the "porous growth" and "hard core-soft shell" methods in Section 3.2.

3.1 | Modeling of cement hydration

Hydration products' volume fraction and reactants are related to temperature and hydration time. For ordinary Portland cement (OPC), the hydration reactions occur between the anhydrous clinker phase X (X can be C_3S, C_2S, C_3A, C_4AF) and water as described below (Jennings, 2000; S. Yang et al., 2021):

$$2C_3S + 6H \rightarrow C_3S_2H_3 + 3CH \quad (11)$$

$$2C_2S + 4H \rightarrow C_3S_2H_3 + CH \quad (12)$$

$$C_3A + C\bar{S}H_2 + 10H \rightarrow C_4A\bar{S}H_{12} \quad (13)$$

$$C_4AF + 2CH + 2C\bar{S}H_2 + 18H \rightarrow C_8A\bar{S}H_{24} \quad (14)$$

According to the nucleation and growth kinetic laws, the reaction rate of a sole clinker phase $\frac{d\zeta_X}{dt}$ can be linked with the driving force as follows:

$$\tau_X \frac{d\zeta_X}{dt} = \tilde{A}(\zeta_X) \quad (15)$$

where ζ_X is the hydration degree of specific clinker phase X, $\tilde{A}(\zeta_X)$ is a normalized affinity, and τ_X (h) is the characteristic time related to the temperature T (K).

TABLE 1 Parameters used in the reaction kinetic model (Bernard et al., 2003; Venkovic et al., 2013).

Clinker	w/c	Avrami model $\tau_X(T_0)$ [h]	κ[1]	$\zeta_{X,0}$ [1]	Diffusion mode $D_X \times 10^{-10}$	ζ_X^*	Activation energy E_{aX}/R[K]
C_3S	0.3	13.5	1.86	0.02	0.42	0.60	4500
	0.4	12.7	1.79		1.05		
	0.5	11.9	1.72		2.64		
	0.6	11.2	1.69		6.42		
	0.7	10.5	1.66		15.6		
C_2S	0.3	71.2	1.10	0.00	6.64	0.60	2500
	0.4	66.1	1.03		6.64		
	0.5	60.9	0.96		6.64		
	0.6	59.8	0.90		6.64		
	0.7	58.6	0.84		6.64		
C_3A	0.3	57.7	1.14	0.04	2.64	0.60	5500
	0.4	53.5	1.07		2.64		
	0.5	49.2	1.00		2.64		
	0.6	42.6	0.93		2.64		
	0.7	35.9	0.86		2.64		
C_4AF	0.3	27.0	2.44	0.04	0.42	0.60	4200
	0.4	24.2	2.37		1.05		
	0.5	21.4	2.30		2.64		
	0.6	17.9	2.23		6.42		
	0.7	14.3	2.16		15.6		

For cement hydration, the influence of temperature on τ_X can be expressed as (Bernard et al., 2003):

$$\tau_X(T) = \tau_X(T_0) \exp\left[\frac{E_{aX}}{\mathcal{R}}\left(\frac{1}{T_0} - \frac{1}{T}\right)\right] \quad (16)$$

The activation energy is presented by E_{aX} (J/mol) in each chemical reaction of clinker phase X, T_0 presents the constant reference temperature (293K).

The normalized affinity $\tilde{A}(\zeta_X)$ in Equation (15) relies on the reaction processes. There are at least three processes for cement hydration: dissolution process, growth and nucleation process, and diffusion process.

(1) The dissolution process occurs during the induction period and lasts for a relatively short time. The normalized affinity $\tilde{A}(\zeta_X)$ can be regarded as a constant number 1, thus, $\tau_X = \tau_X(T_0) = \frac{t_{X,0}}{\zeta_{X,0}}$, in which $t_{X,0}$ is the induction period duration and $\zeta_{X,0}$ is the threshold of hydration degree for phase X at the end of the induction period. The values adopted in this study (Bernard et al., 2003; Venkovic et al., 2013) are summarized in Table 1.

(2) Nucleation and growth process follows the dissolution process once $\zeta_{X,0}$ is achieved. The normalized affinity

can be described as

$$\tilde{A}(\zeta_X) = \frac{1 - |\zeta_X - \zeta_{X,0}|}{\left[-\ln\left(1 - |\zeta_X - \zeta_{X,0}|\right)\right]^{(1/\kappa)-1}} \quad (17)$$

The characteristic time at temperature T_0 can be described as

$$\tau_X(T_0) = \frac{1}{\kappa_X \, k_X} \quad (18)$$

where κ_X is the reaction order, and k_X is the rate constant (see Table 1)

(3) Diffusion process occurs when the hydration degree is beyond the value of ζ_X^*. During this period, the hydration reaction kinetics are restricted by the diffusion of ions, which are dissolved from the hydrated layers around the clinkers. During this process, the normalized affinity can be:

$$\tilde{A}(\zeta_X) = \frac{(1 - \zeta_X)^{2/3}}{\left(1 - \zeta_X^*\right)^{1/3} - \left(1 - \zeta_X\right)^{1/3}} \quad (19)$$

with

$$\tau_X(T_0) = \frac{B^2}{3D_X} \quad (20)$$

where D_X is the diffusivity (cm^2/h), and $B = 5 \times 10^{-4}$cm (Bernard et al., 2003) is anhydrous cement particles' mean radius at the beginning.

The relationship between overall hydration degree $\zeta(t)$ of cement paste and clinker hydration degree ζ_X can be calculated as

$$\zeta(t) = \frac{\sum_X m_X \zeta_X(t)}{\sum_X m_X} \quad (21)$$

where m_X is the X clinker phases' mass fraction in the cement.

During the hydration process, the cement paste consists of crystals, anhydrous clinkers, C-S-H, and pores. Functions of time and hydration degree can be used to calculate the volumes of the main clinkers (V_X) and the hydrated products (V_i) as

$$V_X(t) = \frac{m_X}{\sum_X m_X}\left(1 - \zeta_X(t)\right)V_c^0 \quad (22)$$

$$V_i(t) = \frac{M_i}{M_X}\frac{\rho_X}{\rho_i}m_X N_i^X \zeta_X(t) V_c^0 \quad (23)$$

the index i indicates the hydration products i (C-S-H or crystals); N_i^X is the moles of products hydrated by one mole of clinker phase X after hydration and can be obtained through stoichiometric analysis as Equations (11)–(14); M_X

and M_i are mole mass of clinkers and hydration products, while ρ_X and ρ_i are the density of clinkers X and hydration products i; V_c^0 is the cement's initial volume. Under the certain w/c, the total volume V_{tot} is given as $V_c^0 \times (1 + \frac{\rho_c}{\rho_w} \times (w/c))$ without the consideration of shrinkage, and $f_X = \frac{V_X}{V_{tot}}$ or $f_i = \frac{V_i}{V_{tot}}$ presents the volume fractions of anhydrous clinker phases and hydration products. Pore's volume fraction can be calculated as $f_p = 1 - \sum_X f_X - \sum_i f_i$. The relevant parameters adopted for calculating volume fractions are given in Table 2.

During the hydration process, it is reported that C-S-H precipitated during the diffusion process has a higher density than those related to dissolution and nucleation stages (Achour et al., 2020; Constantinides & Ulm, 2007). Therefore, HD and LD C-S-H can be distinguished through different hydration stages. The crystals are also divided into micro- and nano-sized ones related to the HD and LD C-S-H portions. Moreover, the pore structure is clarified as three groups within different scales. Section 2 illustrates that LCPs are the pore space between different hydrated cement clinkers. Small capillary pores are the pore space within LD C-S-H gels at the outer layer. The gel pores are interspace between C-S-H particles at different layers. Thus, the subdivision of crystals and pores can be calculated by the following equations:

Crystals:

$$f_{mc} = \eta f_{Cy} \quad (24)$$

$$f_{nc} = (1 - \eta)f_{Cy} \quad (25)$$

$$\eta = \frac{f_{ldcsh}}{f_{ldcsh} + f_{hdcsh}} \quad (26)$$

Pores:

$$\rho_{ldcsh} = \frac{f_{ldcsh}^{gel\ pore}}{f_{ldcsh}} = 0.37 \quad (27)$$

$$\rho_{hdcsh} = \frac{f_{hdcsh}^{gel\ pore}}{f_{hdcsh}} = 0.24 \quad (28)$$

$$f_{scp} = \frac{\rho_{ol}}{1 - \rho_{ol}}(f_{mc} + f_{ldcsh}) \quad (29)$$

$$f_{lcp} = f_p - f_{scp} - f_{gel\ pore} \quad (30)$$

where f_{mc} and f_{nc} represent the micro- and nano-sized crystals' volume fractions, respectively; η is the volume fraction of micro-crystals in total crystals' volume, f_{Cy}; f_{ldcsh} and f_{hdcsh} are the volume fraction of LD and HD C-S-H, respectively; f_p, f_{lcp}, f_{scp}, and $f_{gel\ pore}$ are the volume fraction of total pores, LCPs, SCPs, and gel pores, respectively; ρ_{ldcsh}, ρ_{hdcsh}, and ρ_{ol} are porosities of LD C-S-H,

TABLE 2 The relevant parameters for determining the volume fraction (Bernard et al., 2003).

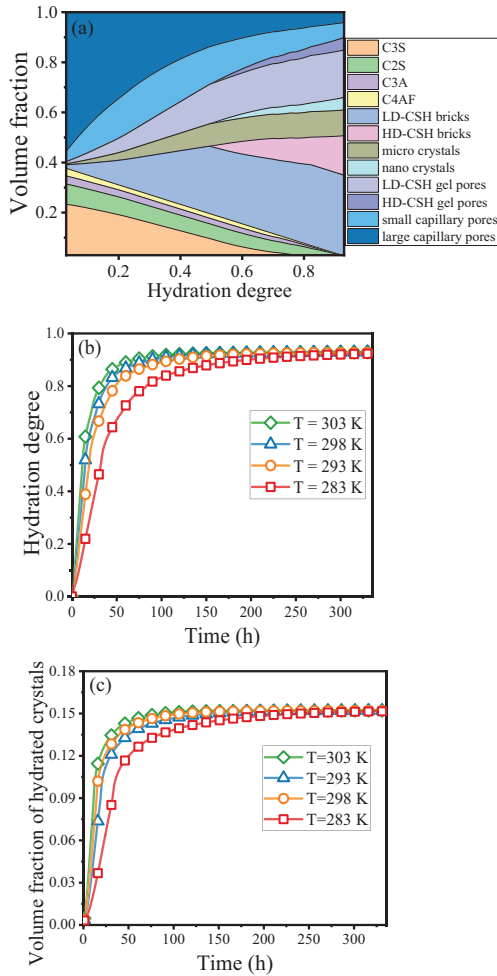| Symbol [unit]	Reactants						Products	
	C_3S	C_2S	C_3A	C_4AF	w	c	C-S-H	Crystals
ρ [g/cm^3]	$\rho_c \frac{m_{C_3S}}{\sum_X m_X}$	$\rho_c \frac{m_{C_2S}}{\sum_X m_X}$	$\rho_c \frac{m_{C_3A}}{\sum_X m_X}$	$\rho_c \frac{m_{C_4AF}}{\sum_X m_X}$	1	3.15	2.04	2.24
M[g/mol]	228.32	172.24	270.20	430.12	18	$\sum_X m_X M_X$	227.2	74
N_{C-S-H}^X[1]	1.0	1.0	–	–				
N_{Cy}^X[1]	5.3	4.3	10.0	10.75				

FIGURE 4 Changes in (a) volume fraction of different phases at different hydration degrees $T = 293$ K, (b) hydration degree, and (c) volume fraction of crystals at different temperatures over time.

HD C-S-H, and outer layer, respectively (Constantinides & Ulm, 2007).

According to the cement database provided by cement producers (Constantinides & Ulm, 2004), Figure 4a displays the calculated volume fraction of different components for type I OPC as an illustrative example, where $w/c = 0.5$, $T = 293$K, $m_{C_4AF} = 0.073$, $m_{C_3A} = 0.076$, $m_{C_2S} = 0.187$, $m_{C_3S} = 0.543$. It is clear to find from the suspension area diagram that with the cement

clinkers consuming, more and more pore spaces are occupied with the increased volume of hydrated products. The total porosity, which concludes the gel pores, SCPs, and LCPs, is approximately 33.03%, near the data measured by Constantinides and Ulm (2004) as 39.7% under the same conditions. Figure 4b shows the relationship between time and hydration degree under different temperatures T. It indicates that the hydration degree goes up quickly at the beginning of hydration and then approaches relatively steady. The terminal hydration degree is predicted as 0.90, consistent with the experimental data given by Ma et al. (2014) with 0.89. As shown in Figure 4c, it can be found that increasing the temperature will promote the hydration process, and the volume fraction of the hydration product will change quickly at early ages.

3.2 | Microstructure generation

Based on the calculated volume fractions of different phases under specific reaction conditions (including w/c, temperature and time), two procedures, "porous growth" and "hard core-soft shell" method, are proposed in this section to generate 3D microstructure at different scales, including Scale 1 (cement paste), Scale 2-1 (outer layer), and Scale 2-2 (inner layer). The flowchart and schematics of the generation procedures of 3D voxel-based microstructures at different scales are shown in Figure 5.

For Scale 1, M. Zhang et al. (2012) reported that a minimum size of $100^3 \mu m^3$ is required to analyze the diffusivity of cement paste. Based on this, the RVE size for Scale 1 is selected as $100^3 \mu m^3$. Furthermore, given that 100 nm is typically used to distinguish between small capillary pores at Scale 2-1 and LCPs at Scale 1, as discussed in Section 2, a resolution of 100 nm/voxel is adopted for Scale 1. As shown in Figure 5a-1, the initial unhydrated cement paste will be modeled using randomly distributed spheres representing cement particles within the RVE and applying periodic boundary conditions. The cement particle size distribution is assumed to follow the Rosin–Rammler distribution (Huang et al., 2015; Maekawa, 2008). Then, the initial RVE, including the cement particles, is digitized into a voxel-based system comprising 1000^3 voxels.
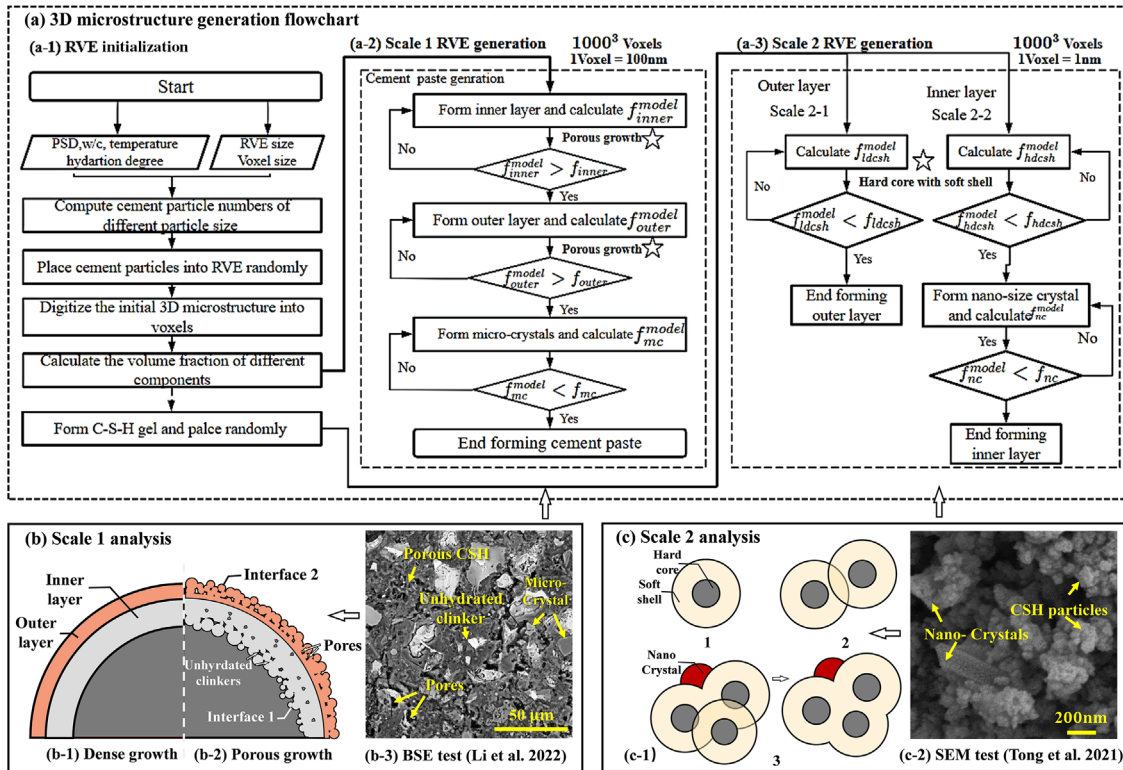
FIGURE 5 Flowchart and schematics of the algorithm generation of voxel-based microstructure at different scales. Flowchart of (a-1) RVE initialization, (a-2) Scale 1 generation, and (a-3) Scale 2 generation; schematic analysis of (b-1) dense growth, (b-2) porous growth and (b-3) backscattered electron (BSE) test at Scale 1; schematic analysis of (c-1) hardcore-softshell growth and (c-2) scanning electron microscope test at Scale 2.

During hydration modeling, the volume fraction of different hydration products can be calculated as illustrated in Section 3.1 considering the *w/c*, temperature, chemical composition, and hydration time. To simulate the formation of inner and outer hydration products, as shown in Figure 5b-1, it is generally assumed that concentric layers of hydrates with sub-voxel porosity "grow densely" around cement particles, as done in the HymoStruc model and *μic* model (Thomas et al., 2011). However, backscattered electron (BSE) image from L. Li et al. (2022), as depicted in Figure 5b-3, reveals that hydration products around unhydrated cement particles are porous and contain embedded pores. In other words, hydration products are blended with LCPs. Therefore, this study proposes a "porous growth" method. As illustrated in Figure 5b-2, small spheres representing hydration products will generate inward from Interface 1 to model the generation of the inner layer. This process will continue until the inner layer's volume fraction (f_{inner}) is reached. Similarly, the outer layer will grow outward from Interface 2 until the target volume fraction (f_{outer}) is achieved as illustrated in Figure 5a-2. During the process, the outer layers of different cement particles may come into contact, leading to continuous updates of Interfaces 1 and 2. This approach allows pores to blend with

the outer layer and unhydrated clinkers to merge with the inner layer, aligning more closely with BSE test observations. Next, according to f_{mc}, the micro-sized crystals (different types of crystals are not distinguished here) are randomly placed in contact with the outer layer. Through this, the microstructure of cement paste (Scale 1) can be generated. At this scale, LCPs are visually represented, while the inner and outer layers are treated as homogeneous phases of solids hydration products and smaller pores.

$$f_{\text{inner}} = f_{\text{nc}} + f_{\text{hdcsh}} + f_{\text{hdcsh}}^{\text{gel pore}} \tag{31}$$

$$f_{\text{outer}} = f_{\text{scp}} + f_{\text{ldcsh}} + f_{\text{ldcsh}}^{\text{gel pore}} \tag{32}$$

For Scale 2, further classification of the inner and outer layers is necessary to visually present gel and small capillary pores. The RVE sizes of Scales 2-1 and 2-2 are set as 1000^3 nm with a resolution of 1 nm/voxel. As shown in the scanning electron microscope image by Tong et al. (2021) in Figure 5c-2, individual C-S-H particles within C-S-H gels can be approximated as spheres, with some nano-crystals embedded within the gels. To simulate the inner and outer layers, C-S-H particles are modeled as spheres with an impenetrable hard core surrounded by a
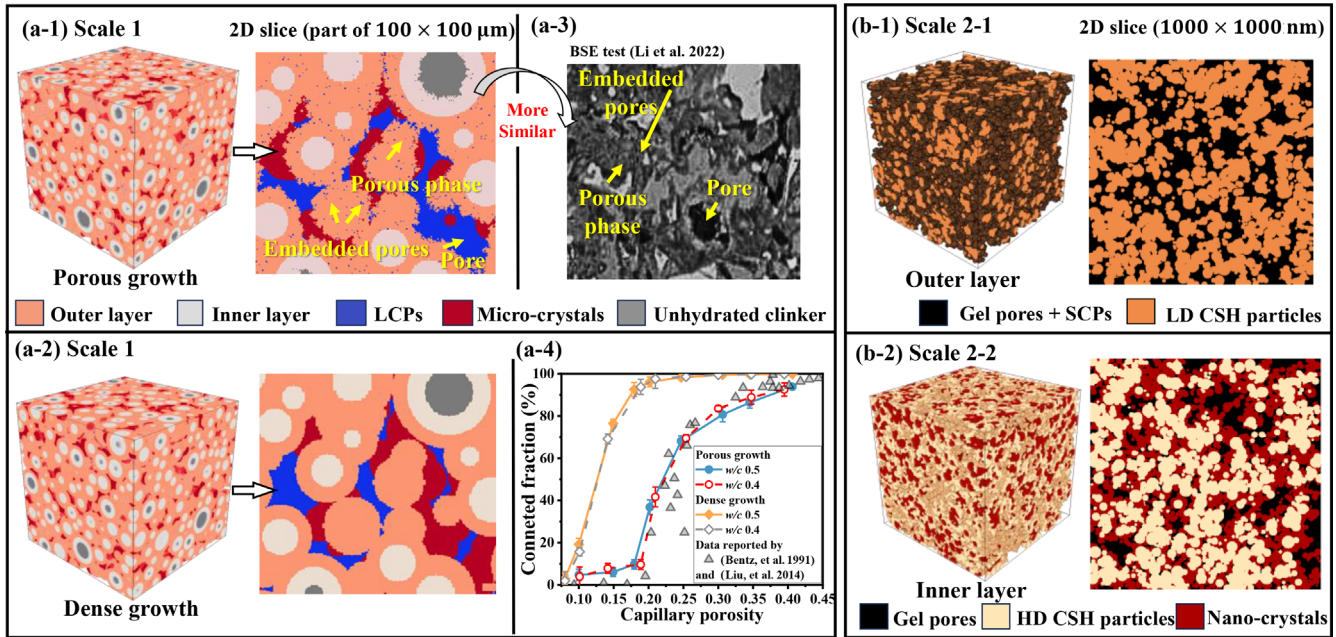
FIGURE 6 Image of voxel-based cement paste. Three-dimensional (3D) and two-dimensional (2D) illustration of generated RVE at Scale 1 by (a-1) porous growth method, (a-2) dense growth method, (a-3) BSE image of cement paste, and (a-4) comparison of connected fraction of capillary pores. 3D and 2D illustration of generated RVE at (b-1) Scale 2-1 and (b-2) Scale 2-2.

TABLE 3 Size of microscopic phases used in generating representative volume elements (Achour et al., 2020; Haecker et al., 2005).

Cement paste		Outer layer		Inner layer	
Particles	1–50 μm	CSH particles	5–60 nm	CSH particles	5–60 nm
Micro-size crystals	1–10 μm			Nano-size crystals	< 1 μm

soft shell, with a size ratio of 2:3, as depicted in Figure 5c-1. To accurately represent the growth of C-S-H, no isolated particles should appear (Scherer, 1999), requiring C-S-H particles to overlap with one another. During generation, the soft shell of a newly introduced C-S-H particle can freely overlap with the soft shells or hard cores of existing C-S-H particles, while the new hard core can only overlap with existing soft shells. For Scale 2-1, this process continues until the volume fraction of LD C-S-H (f_{ldcsh}) is reached as illustrated by Figure 5a-3. For Scale 2-2, nano-crystals are embedded in HD C-S-H gels to form denser inner layers as illustrated by Figure 5a-3. The size of the different phases used for generating cement paste, inner, and outer layers are listed in Table 3.

The type I OPC is again taken as an example (w/c 0.5, $T = 293$K). The generated microstructures for Scale 1 (cement paste) and Scale 2 (two layers) are presented in Figure 6. In Figure 6a-1, a-2, the edges of the hydration products in the RVE generated using the "porous growth"

method are visibly more irregular in shape, compared to those produced by the "dense growth" method. Additionally, some pores are embedded within the porously generated phases, making the microstructure more closely resemble the BSE image shown in Figure 6a-3. After 10 repetitions, the average connected fraction of capillary pores in RVEs with different w/c ratios and capillary porosities, generated by "porous" or "dense" growth method, is shown in Figure 6a-4. The percolation threshold of capillary pores in RVEs generated by the "dense growth" method is approximately 10%, whereas in the RVEs generated by the "porous growth method," it is around 20%. The good agreement between the modeled fraction by "porous growth" method and the data reported by Bentz and Garboczi (1991) and Z. Liu et al. (2014) further indicate that the proposed method can generate a more reliable microstructure. For Scale 2, a comparison of Figures 6b-1,b-2 also reveals that the inner layer is denser than the outer layer.

Based on the multi-scale generated microstructures, Sub-model I will be proposed in Section 4 to extract the corresponding PSDs $p(r)$. Then, pore size-related chloride diffusion coefficient $D(r)$ will be predicted considering the PSDs in Section 5.

4 | SUB-MODEL I: PSD MODEL

The void spaces left in the voxel-based RVEs of Scales 1 and 2 are classified into gel pores, SCPs and LCPs, as marked in
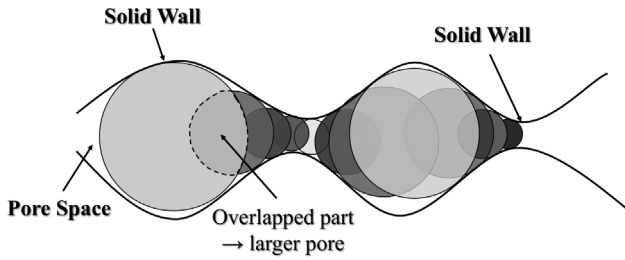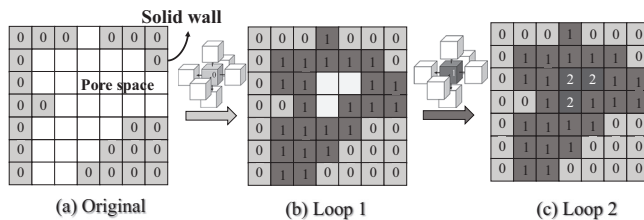
FIGURE 7   A 2D schematic of the pore structure.

FIGURE 8   Procedure 1: Map distance calculation (2D illustration).

FIGURE 9   Procedure 2: Pore size identification (2D illustration). (a) Circle generation and (b) remark voxels.

FIGURE 10   Example of pore structure extraction of the cement paste (Scale 1, $w/c = 0.5$, capillary porosity 40%). Irregular pore structure: (a-1) 3D (a-2) 2D; illustration of pore structure after Procedures 1 and 2: (b-1) and (c-1) 3D, (b-2) and (c-2) 2D.

Figure 6. The pore structure is irregular and arbitrary. This section is going to propose a PSD model to determine the pore sizes over different ranges.

Regardless of different hydration products or anhydrous clinkers, the voxels can be simply clarified as solid or pore voxels (Wan et al., 2024). The arbitrary pore structure can be regarded as a connection of different sizes of pores as shown in Figure 7. All these pores just touch the edge of the solid or boundary. Overlapping areas between larger and smaller pores are attributed to the larger pores. Based on this principle, a voxel-based algorithm that incorporates two procedures is adopted in this sub-model to determine PSDs (Blunt et al., 2013; Raeini et al., 2017): (1) Procedure 1: Calculate the distance map; (2) Procedure 2: Identify the void voxel into different pore groups.

Procedure 1 is used to find the shortest distance between the solid wall and each pore voxel. A 2D schematic of the Procedure 1 is shown in Figure 8. At the beginning, all the solid voxels are marked with the number 0, while pore voxels are marked with NAN. After the first search, the pore voxels nearing the solid voxel are remarked with the number $1(0 + 1 = 1)$. In the next step, the pore voxel nearing the voxel marked with Number 1 will be marked with $2(1 + 1 = 2)$. This process will be repeated until all the voxels are filled with the specific number. It should be noted in the ith loop, if the connected voxels have already been marked with j, the number j will be maintained when $j < i$ and renewed as i when $j > i$. The number marked in each voxel is thus the shortest distance between this pore voxel and the solid wall. It can also be found that the central voxel of larger pore areas will be marked with bigger numbers, compared with smaller pores.
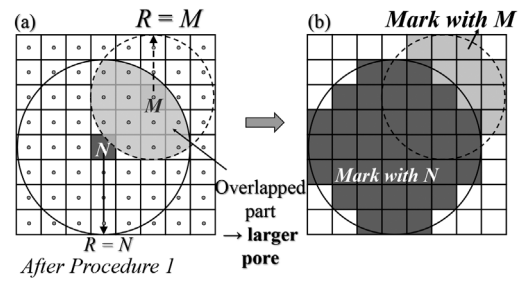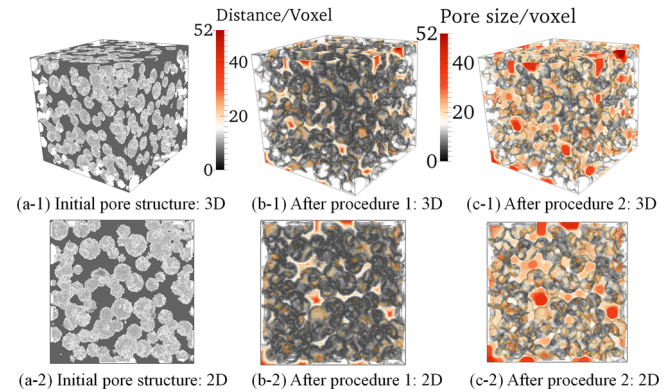
In the subsequent Procedure 2, pore volumes of different pore size groups will be counted. To achieve this, a 2D schematic of the abovementioned Procedure 2 is shown in Figure 9. First, as shown in Figure 9a, a circle will be generated at the center of each voxel. The circle radius equals the marked number obtained from Procedure 1. Numbers N and M ($N > M$) are taken as an example in Figure 9. Subsequently, all pore voxels whose central position falls in the range of the generated circles will be remarked as shown in Figure 9b. For the voxels located in the overlapped area, the overlapped pore voxels belong to larger pores according to the principle mentioned in Figure 7.

Still taking the microstructure of type I OPC and $w/c = 0.5$, $T = 293$K with 40% capillary porosity as an example. Figure 10a-1,a-2 displays the 3D and 2D slices of extracted irregular pore structure of cement paste. Figure 10b-1,b-2,c-1,c-2 shows the pore structure after two procedures. It can be seen that the arbitrary pore structure has been divided into a bunch of pores after two procedures.

Counting the number of voxels presenting different pore sizes, the extracted PSD of generated microstructures is displayed in Figure 11. The PSD shows a peak. Combining
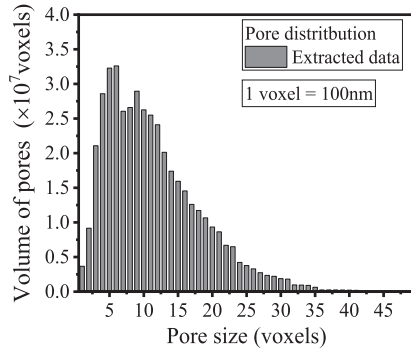
FIGURE 11 Extracted PSD (Scale 1 and $w/c = 0.5$, an example).

PSD extracted from the generated microstructure at Scales 1, 2-1, and 2-2, the multi-modal PSD can be finally obtained. Through this sub-model, the PSD of each scale can be extracted. Section 6.1 will verify the extracted multi-modal PSDs.

5 | SUB-MODEL II: LATTICE DIFFUSION MODEL

After extracting the multi-modal PSDs according to Section 4, if the chloride diffusion coefficient D is also known, the pore size-related diffusion coefficient $D(r)$ can be expressed as the function of multi-modal PSDs $p(r)$ and chloride diffusion coefficient D. At the pore scale, it is reliable to assume that finer pores exhibit lower diffusion coefficients. However, considering that only connected pore systems are functional to transport ions, connectivity and tortuosity are essential parameters for evaluating the transport properties. Consequently, the diffusion coefficient should not be linear with respect to the pore radius. The relationship between pore sizes and the permeability of cement pastes has been explored by many experimental and numerical studies (Xiong et al., 2023). Still, limited work has been carried out on the diffusion coefficient. The formula suggested by Roy (1988) was adopted in the present study, in which the relationship is considered between chloride diffusion coefficient and averaged pore radius:

$$D(r) = k \frac{\log\left(\frac{r}{r_{\min}}\right)}{\log\left(\frac{r_a}{r_{\min}}\right)} D \qquad (33)$$

$$\int_{r_{\min}}^{r_{\max}} D(r) p(r) dr = D \qquad (34)$$

where $r_{\min}$ is the smallest pore radius with $D(r_{\min}) = 0$, r_a corresponds to the averaged peak pore radius as
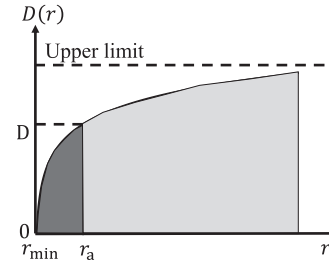

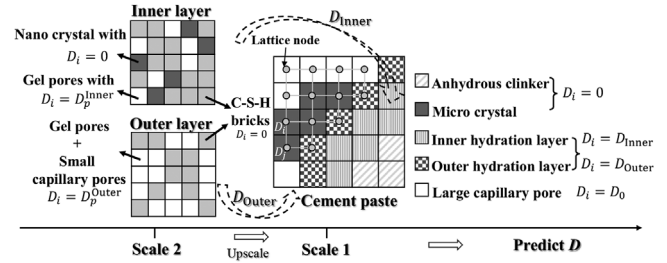**FIGURE 12** Relationship between chloride diffusivities and pore sizes.

FIGURE 13 Diffusion lattice network (2D illustration).

$r_a = \sum_{i=1}^3 \gamma_i B_i$ and $D(r_a) = kD$. The constant k is used to adjust the Equation (33) to fit Equation (34) and is given by:

$$k = \frac{D}{\int_{r_{\min}}^{r_{\max}} \frac{\log(r) - \log(r_{\min})}{\log(r_a) - \log(r_{\min})} p(r) dr} \qquad (35)$$

As shown in Figure 12, it is reasonable that the smaller the pores, the lower the diffusion coefficient, and there is an upper limit for the diffusion coefficient at infinity pore size. This is consistent with common sense that ions own the largest speed when the influence of obstacles can be ignored, just like diffusing in free water.

Thus, to propose the function of the pore size-related diffusion coefficient, it is evident that D must be obtained first. Considering the effect of different pore sizes on chloride diffusivity, Sub-model II will be developed in this section to predict D based on the microstructures generated in Section 3.

The voxel-based microstructures consist of different hydration products and anhydrous clinkers. To map the voxel-based microstructure to a diffusion network, the central point of each voxel is considered a lattice node as shown in Figure 13 (2D schematic). Each lattice node i is given a chloride diffusivity D_i, and due to that different voxels represent different phases; thus, the corresponding nodes own different D_i. As shown in Figure 13, the anhydrous clinker, crystals (micro-sized and nano-size), and C-S-H particles are assumed to be impenetrable ($D_i = 0$). According to Achour et al. (2020), gel pores in the inner and outer layers have different diffusivities:
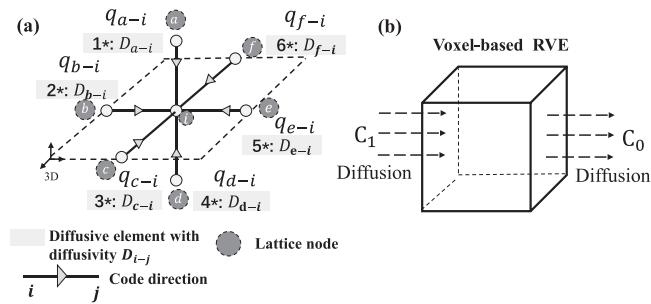
FIGURE 14 A schematic diagram of steady state chloride diffusion (a) flux at each node and (b) diffusion direction and boundary condition.

$D_p^{\text{Inner}} \approx 1.6 \times 10^{-3} D_0$ and $D_p^{\text{Outer}} \approx 4.4 \times 10^{-4} D_0$. D_0 is the diffusion coefficient of chloride ions in free water with $D_0 = 2.03 \times 10^{-9} \text{m}^2/\text{s}$. In this 3D multi-scale model, the diffusivities of the inner and outer layers are obtained first before upscaling to the cement paste Scale 1. Thus, in Scale 1, the diffusion coefficients of pores in the inner and outer layers are defined as D^{Inner} and D^{Outer}, respectively.

It is assumed that voxel-based cement paste is saturated, and diffusion occurs between the face-to-face of different voxels. Correspondingly, in the lattice diffusion network, each node has six connected diffusive elements as shown in Figure 14a. The diffusion coefficient D_{i-j} is given by L. Liu et al. (2013):

$$D_{i-j} = \frac{2D_i D_j}{D_i + D_j} \qquad (36)$$

where D_i and D_j are the ionic diffusion coefficient of lattice node i and j, respectively.

In this way, the voxel-based microstructure can be transformed into a lattice diffusion network. Then, chloride diffusivity D can be predicted based on the steady-state diffusion modeling through the proposed lattice diffusion network. To focus on the intrinsic effect of microscopic features on ionic transport, chloride binding and the changes in pore topology are not considered in the steady-state modeling of chloride diffusivity prediction.

At the steady state, the ionic diffusion process in cementitious materials can be determined by Fick's first law (Freeman et al., 2019; C. Liu & Zhang, 2022); thus, the flow along the element $i - j$ can be described as

$$q_{i-j} = -D_{i-j} \frac{\Delta c_{i-j}}{\Delta x} \qquad (37)$$

Here, q_{i-j} presents the flow density along the diffusive direction $i - j$, $\frac{\Delta c_{i-j}}{\Delta x}$ is the concentration gradient between the face-to-face lattice nodes. It should be noted that if

either D_i or D_j is zero, D_{i-j} should be zero as well. During the modeling, q_{i-j} is positive for inflow and negative for outflow. Refer to the concept of "element stiffness matrix," the "element diffusive matrix" for a diffusive lattice element $i - j$ can be:

$$-\frac{D_{i-j}}{\Delta x} \begin{bmatrix} 1 & -1 \\ -1 & 1 \end{bmatrix} \begin{bmatrix} c_i \\ c_j \end{bmatrix} = \begin{bmatrix} q_{i-j} \\ q_{j-i} \end{bmatrix} \qquad (38)$$

It is known that the diffusion process converts from a non-steady state to a steady state, and the outlet flux of ions increases over time. Once a steady state is achieved, the flux remains constant. Therefore, for each node, the inlet flux equals the outlet flux and remains unchanged over time. As depicted in Figure 14a, in a steady state, the concentration of the node i can be directly calculated using the following equations:

$$\sum_{j=a}^{f} D_{j-i} (C_j - C_i) = 0 \qquad (39)$$

$$C_i = \frac{D_{a-i}C_a + D_{b-i}C_b + D_{c-i}C_c + D_{d-i}C_d + D_{e-i}C_e + D_{f-i}C_f}{D_{a-i} + D_{b-i} + D_{c-i} + D_{d-i} + D_{e-i} + D_{f-i}} \qquad (40)$$

The neighboring nodes $j = a, b, c, d, e, f$ surround node i, $D_{a-i}, D_{b-i}, D_{c-i}, D_{d-i}, D_{e-i}$ and D_{f-i} represents the diffusivities of diffusive element $a - i$, $b - i$, $c - i$, $d - i$, $e - i$, $f - i$, respectively.

Assembling elements one by one, the complete "diffusive matrix" equation for the generated microstructure can be obtained. The diffusive matrix is symmetric and sparse. In order to solve this large system, an iterative method is more suitable than a direct solution. In this study, the conjugate gradient method, one of the iterative methods, is utilized (Jia et al., 2024; C. Liu & Zhang, 2022). To initialize the iterative procedure, the initial chloride concentration of the voxel-based microstructure is set to zero. The binding effect on diffusivity is concluded by the factor f_B in Section 2 and is ignored during the iterative steps. Boundary conditions of concentration are set on the upstream and downstream surfaces with C_1 (1 mol/m³) and C_0 (0 mol/m³) as shown in Figure 14b. As the steady diffusion state is modeled, the set boundary chloride concentrations C_1 and C_0 will not change the predicted intrinsic diffusivities. The iterative steps will continue until the C_i at each voxel is not changed. Once the steady state is achieved, the diffusion coefficient D (m²/s) of cement paste can be determined as

$$D = \frac{Q}{A} \frac{L}{C_1 - C_0} \qquad (41)$$

where Q is the outlet flux (mol/s), L is the sample's length (m), and A is the area of the outlet surface (m²). Through

TABLE 4 Cement chemical compositions (wt %; Huang et al., 2015).

C_3S	C_2S	C_3A	C_4AF
64.24	16.92	7.86	10.76

the diffusion modeling of the generated microstructure, the effect of different pore sizes on chloride diffusion can be directly captured. The comparison of predicted D with experimentally measured data will be presented in Section 6.2.

6 | COMPARISON OF MODELED AND EXPERIMENTAL RESULTS

Based on the generated multi-scale microstructures, multi-modal PSDs and pore size-related diffusivity can be determined through two sub-models. To verify the proposed framework, this section will first compare the modeled results from sub-models with experimental data in Sections 6.1 and 6.2. Then, combining $p(r)$ and $D(r)$, the multi-scale chloride transport model described in Section 2 will be verified against experimental data in Section 6.3. To reduce chance error, each validation was repeated 10 times.

6.1 | Extracted PSDs from Sub-model I

The third-party experimental results used to prove the Sub-model I are obtained from Huang et al. (2015). In the literature, the researchers tested the PSDs with different w/c. So, it can be a suitable data source to prove the proposed sub-model. In the tests, the cement phase's chemical composites are given in Table 4. At 293K, 110 days were cured before measuring the PSD of specimens by MIP. The w/c ratios 0.5 and 0.7 are adopted for comparison. Different phases' volume fractions after 110 days of hydration can be obtained firstly, according to Section 3.1, and the microstructure can be generated through the flowchart illustrated in Section 3 as shown in Figure 15. In Figure 15a-1–f-1), it is obvious that the generated pore structure has an arbitrary geometry, and the microstructure becomes much denser with lower w/c. Figure 15a-2–f-2 shows the extracted pore sizes after two procedures of Sub-model I.

By counting the number of voxels presenting different pore sizes at multi-scales, multi-modal PSD can be obtained. Figure 16 shows a good agreement between extracted multi-modal PSDs and experimental results, suggesting that the distribution of widely ranged pores can be determined through the proposed Sub-model I.
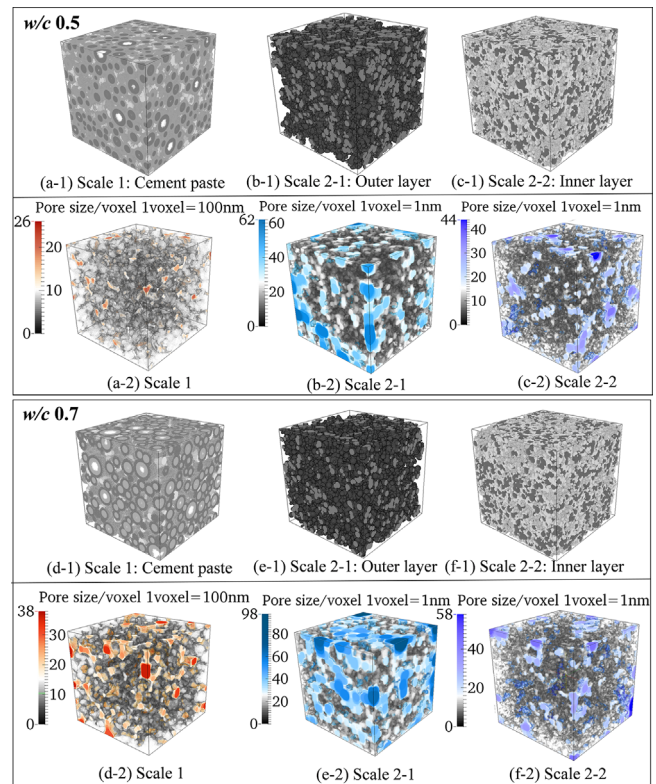

FIGURE 15 Generated RVEs and extracted pore sizes. Generated microstructures, $w/c = 0.5$: (a-1) Scale 1, (b-1) Scale 2-1, (c-1) Scale 2-2; $w/c = 0.7$: (d-1) Scale 1, (e-1) Scale 2-1, (f-1) Scale 2-2; extracted pore sizes: $w/c = 0.5$: (a-1) Scale 1, (b-1) Scale 2-1, (c-1) Scale 2-2; $w/c = 0.7$: (d-1) Scale 1, (e-1) Scale 2-1, (f-1) Scale 2-2.
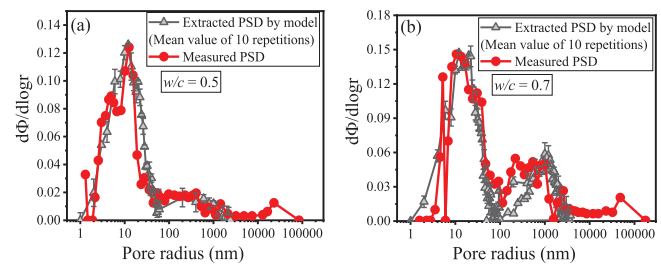
FIGURE 16 Comparison of extracted (average results of 10 repetitions with error bars) and experimentally measured PSD (a) $w/c = 0.5$ and (b) $w/c = 0.7$.

6.2 | Predicted diffusivities from Sub-model II

To verify the proposed lattice diffusion model, herein, third-party tested chloride diffusion coefficients D_t of different w/c are compared with the predicted D (Luping & Nilsson, 1993b; Ngala et al., 1995; Page et al., 1981; Yu & Page, 1991). Modeled microstructures are generated with the consideration of the chemical compositions and hydration time. The cement components

TABLE 5 Third-party experimental measurements of chloride diffusivities in bulk cement paste.

Reference	w/c	D_{test} $(10^{-12} \text{m}^2/\text{s})$	Curing condition	Chloride concentration	Test time
Page et al. (1981)	0.4	1.99	60 days in saturated Ca(OH)$_2$ solution	1 mol/L	3 weeks
		2.06			
		2.96			
	0.5	4.06			
		4.47			
		4.82			
	0.6	11.0			
		12.4			
		15.6			
Ngala et al. (1995)	0.4	3.65	70 days in 0.035 mol NaOH solution	1 mol/L	3–5 days
		3.95			
		4.35			
	0.5	7.16			
		7.8			
		8.06			
	0.6	10.4			
		12.6			
		17.8			
Yu and Page (1991)	0.35	1.09	70 days in 0.035 mol NaOH solution	1 mol/L	3 days
	0.5	5.44			
	0.6	9.93			
Luping and Nilsson (1993b)	0.4	2.92	2 weeks in saturated Ca(OH)$_{2aq}$	1 mol/L	2 weeks
	0.6	9.44			
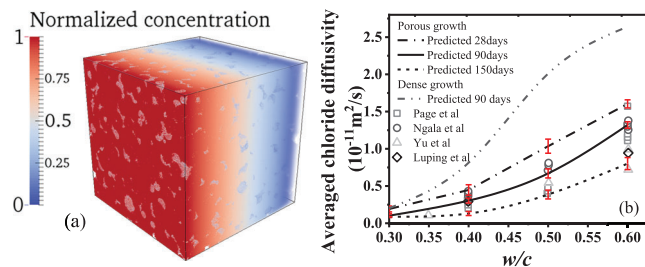
FIGURE 17 Results of (a) normalized concentration distribution at the steady-state diffusion, (b) predicted chloride diffusion coefficient with different w/c ratios (average results of 10 repetitions with error bars).

used for microstructure generation and diffusion coefficient prediction are CEM I 42.5 with mass fraction: $m_{C_4AF} = 9\%$, $m_{C_3A} = 8.43\%$, $m_{C_3S} = 63.53\%$, $m_{C_2S} = 13\%$ (M. Zhang et al., 2012). Table 5 lists the experimental data. The modeled temperature is set as 293K.

The normalized chloride concentration distribution at the steady state is shown in Figure 17a with w/c of 0.5. Based on Equation (41), diffusion coefficients at different w/c can be predicted, and the comparison of modeled and

measured results is illustrated in Figure 17b. The predicted D increased with the increasing w/c due to higher porosity. Based on the RVEs generated by the "porous growth method," an acceptable correlation is shown between the modeled and measured results in a reasonable range. On the contrary, based on the RVEs generated by the "dense growth method," the predicted chloride diffusivity will be overestimated, which is caused by the higher connected fraction of capillary pores, as illustrated in Figure 6a-4. This indicates that the effect of pore structure connectivity on the ionic diffusion coefficient of cement paste can be better revealed through the proposed "porous growth" microstructures.

6.3 | Predicted penetration depths from multi-scale chloride transport model

Through the above two sub-models, the required parameters for multi-scale chloride transport model, $p(r)$ and $D(r)$, can be determined. To verify the multi-scale chloride model as illustrated in Section 2, the predicted chloride penetration depths under electrical potential by the

TABLE 6 Experimental information (Spiesz & Brouwers, 2012).

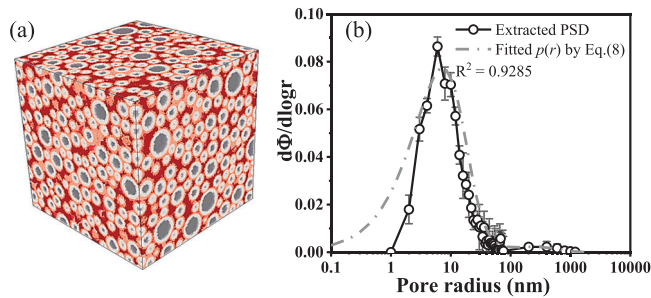| Items	Parameters
Cement composition	$m_{C_3S} = 0.7038, m_{C_2S} = 0.126,$ $m_{C_3A} = 0.117, m_{C_4AF} = 0.0532$
Volume fraction of aggregates	0.5215
w/c	0.3
Curing temperature	293K
Curing time	27 day curing + 1 day saturating
Applied voltages	35, 47.5, 60 V

FIGURE 18 Modeled results considering the experimental settings: (a) generated microstructure of Scale 1($w/c = 0.3$) and (b) extracted and fitted multi-modal PSD (average results of 10 repetitions with error bars).

proposed model are compared with tested data reported by Spiesz and Brouwers (2012). The chloride concentration distributions and the relationship between pore sizes and the chloride transport process can also be investigated. The parameters needed for the abovementioned experiment are given in Table 6. In the experiment, the concretes were cured in water for 27 days and sliced for the rapid chloride migration (RCM) tests. Three different voltages (35, 47.5, and 60 V) were applied and kept constant during the experiments. For each test, the RCM testing process lasted for 7 h.

By inputting the parameters listed in Table 6 into Sub-model I, Figure 18 displays the generated microstructure and extracted PSDs. Parameters ρ_i and B_i present porosity and peak pore size of each pore group, respectively. The relevant ρ_i, B_i, and the predicted chloride diffusion coefficient D are listed in Table 7.

By substituting the predicted PSD $p(r)$ and pore size-related diffusivity $D(r)$ into Equation (10), the multi-scale chloride transport model can be established with further consideration of the effect of chloride binding (f_B), aggregates (f_A), and ITZs (f_{ITZ}). The pore size-related chloride diffusivity of concrete used in Equation (10) should be:

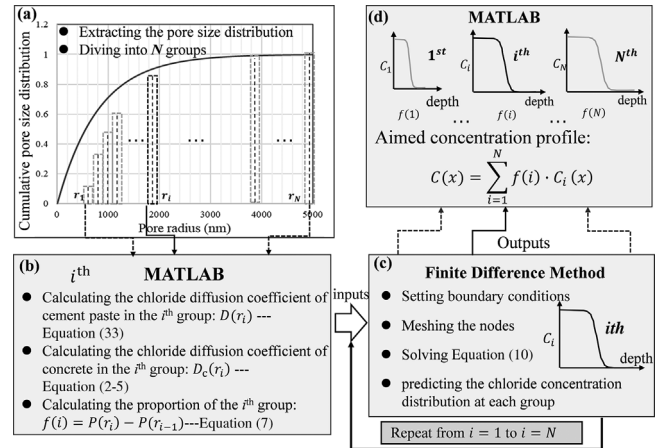$$D_c(r) = f_B \cdot f_A \cdot f_{ITZ} D(r) \qquad (42)$$

FIGURE 19 MATLAB diagram for solving Equation (10). (a) Pore group dividing, (b) calculating parameters of ith group, (c) calculating chloride concentration of ith by FDM, and (d) calculation of aimed chloride concentration profile.

Due to that, Equation (10) involves an integral term, MATLAB (of course other programming languages can be used as well) is utilized to write the code for solving the equation. Considering the pore size-related diffusivity $D(r)$ is independent of depth (x), time (t), and concentration (C), the transport process with diffusivity $D(r)$ described by the integral function can be regarded as the weighted average of several transport processes with different diffusivities D. As explained in Figure 19a, by using the MATLAB, the pore size range $[r_{min}, r_{max}]$ can be divided into N groups. For ith group, the mean pore radius r_i is used for calculating the pore-sized related radius $D(r_i)$ and the fraction of the ith group $f(i)$ as illustrated in Figure 19b. Then, finite difference method (FDM) is coded by MATLAB to predict the concentration distribution with different diffusivities $D_c(r_i)$ as illustrated by Figure 19c. By using MATLAB, the FDM is repeated from $i = 1$ to $i = N$. At last, the aimed chloride concentration profiles can be obtained by calculating the weighted average of concentration as described in Figure 19d.

Figure 20 shows the comparison between modeled and experimental results under different electrostatic potential gradients.

Figure 20a presents the results predicted by the proposed multi-scale chloride transport model, which accounts for the multi-modal PSD $p(r)$ and pore size-dependent diffusivity $D(r)$ as described in Equation (10). Figure 20b shows the results obtained using the reference model, which adopts a single diffusion coefficient D as Equation (1). For the concentration profiles predicted by the present multi-scale transport model, Figure 20a shows that the chloride profiles are relatively smooth, though a slight overestimation of concentration near the surface may be attributed to experimental test errors. On the contrary, the chloride

TABLE 7 Parameters of predicted pore size distribution (PSD).

w/c	ρ_1	B_1 (nm)	ρ_2	B_2 (nm)	ρ_3	B_3 (nm)	D (10^{-12} m^2/s)
0.3	0.1623	6.99 ± 1.2	0.017	17.4 ± 2.8	0.0052	246.4 ± 8.5	2.5
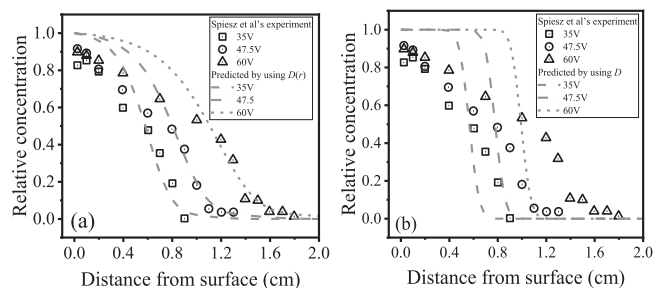
FIGURE 20 Chloride penetration profiles with three different applied voltages (a) chloride concentration predicted with: pore size-related chloride diffusivity $D(r)$ in multi-scale model and (b) chloride concentration predicted with chloride diffusivity D in reference model.

distribution predicted by the reference model shows a sharp front as shown in Figure 20b. This sharp front can be explained by the fact that penetration depth is often related to the fastest transport speed, which is associated with the largest pore size groups. Thus, the reference model considering the single diffusivity D for large and small pores cannot present smooth ion distribution. The predicted chloride penetration depths, considering the pore size effect, are also more consistent with measured data. Under a 60 V potential, the penetration depths of experimental data, predicted results by multi-scale model and predicted results by reference model, are 1.65, 1.63, and 1.2 cm. For different applied electrostatic potential gradients, the prediction error of penetration depths can be reduced by 10% to 25% through the proposed multi-scale chloride transport model. The reduced prediction error indicates that the proposed framework can better capture the effect of pore sizes on the chloride transport process in concrete.

7 | RESULTS AND DISCUSSION

7.1 | Effect of pore size proportions on chloride penetration

To further analyze the effects of PSDs on chloride penetration, the ionic concentration profiles are predicted by adopting different porosities (ρ_1, ρ_2, ρ_3) of three pore groups: pores in the inner layer (group 1), pores in the outer layer (group 2), and LCPs (group 3). The related parameters are given in Table 8, distribution P1 is the extracted PSD carried out in Section 6. For assumed P2 and P3, it is

TABLE 8 Parameters of different proportions of multi-modal PSDs.

	ρ_1	B_1	ρ_2	B_2	ρ_3	B_3	B_{mean}	D
P1	0.1623		0.017		0.0052		14.7	2.5
P2	0.1135	6.99	0.017	17.4	0.0540	246.4	78.1	3.3
P3	0.0148		0.017		0.1527		206	4.0

Note: $B_{mean} = \sum_{i=1}^{3} \gamma_i B_i$.
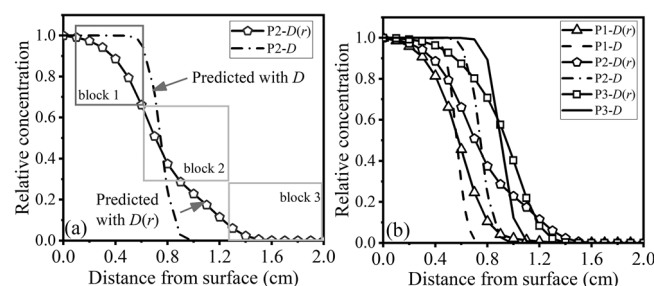
FIGURE 21 Predicted chloride concentration (a) within three regions and (b) with different proportions of three pore groups. *Note*: PX-D represents the transport model with single D, and PX-$D(r)$ represents the proposed model with pore-size-related $D(r)$ (35 V).

supposed that the porosity of LCPs (group 3) is increasing, while the peak radius (B_1, B_2, B_3) and total porosity remain consistent. The temperature and sand fraction used in this section are consistent with those in Table 6. The applied voltage is set as 35 V. The obtained results for chloride concentration under different PSDs are shown in Figure 21.

Figure 21a compares the chloride concentration obtained by the transport model with D and by the proposed multi-scale chloride transport model. According to the slope tendency of chloride distribution curves in Figure 21a, the concentration distribution predicted by the model with $D(r)$ can be divided into three regions. The predicted concentration distribution by D shows a sharp front due to that diffusivities of different pore sizes are assumed as the same. On the contrary, by adopting $D(r)$, the chloride concentration near the surface (the first block region) is related to the proportion of gel pores, which have a relatively lower transport rate, while the concentration in the second and third block regions relate to small and LCPs, which own larger pore sizes and higher diffusivities. Comparing P2-D and P2-$D(r)$, it can be concluded that the influence of gel pores on chloride transport will be overestimated, and the role of larger pores on penetration

depths will be underestimated by adopting the single D in chloride transport model.

Additionally, although the total porosities of P1, P2, and P3 are the same, Figure 21b indicates the chloride penetration can be accelerated by the increased proportion of large pores. The chloride concentration profiles change a lot by altering the pore size proportion of different pore sizes. This indicates the importance of considering varying PSDs in transport modeling rather than single parameters such as total porosity.

7.2 | Comparisons between single-modal and multi-modal PSD

The PSD studied in the present study was represented by a multi-modal R–R distribution model covering a larger range of pores as illustrated in Section 2. This section is going to compare the predicted chloride concentration profiles by model considering multi-scale model considering multi- or single-modal PSD. The multi-modal PSD used in this section is the extracted PSD carried out in Section 6.3. The applied voltage is set as 35 V. Governing equations for the abovementioned three models can be expressed as

(1) Model 1: multi-scale model considering multi-modal PSDs (the model proposed in the present study)

$$\frac{\partial C}{\partial t} = \int_{r_{\min}}^{r_{\max}} \left[D(r) \nabla^2 C + D(r) \frac{FZ}{RT} \nabla (C \nabla \Phi) \right] p(r) \, dr$$

$$(43)$$

where $D(r)$ depends on the multi-modal PSDs as illustrated in Section 2:

$$p(r) = \sum_{i=1}^{3} \gamma_i p_i(r) = \sum_{i=1}^{3} \frac{\gamma_i}{B_i} \exp\left(-\frac{r}{B_i}\right) \qquad (44)$$

(2) Model 2: multi-scale model considering single PSD (reference model)

In Model 3, function $D(r)$ is related to a single PSD with an averaged peak pore radius:

$$p(r) = \frac{1}{B_{\text{mean}}} \exp\left(-\frac{r}{B_{\text{mean}}}\right) \qquad (45)$$

Figure 22 compares the chloride concentration profiles obtained by these two kinds of models. Chloride concentration predicted by the single-modal PSD model shows a relatively sharp front. Compared with experimental results (illustrated in Section 6.3), the model considering single
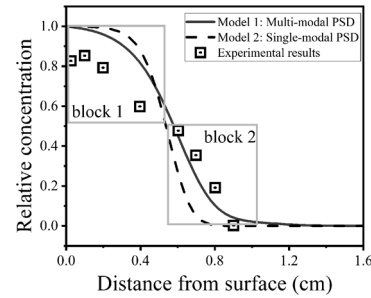

FIGURE 22 Predicted chloride concentration with single and multi-modal PSDs.

PSD will overestimate the concentration near the surface (the first block region) and underestimate the chloride penetration depth (the second block region). Although it is reported that peak pore radius, which presents the pore group with the highest proportion, will have the largest influence on the transport properties (C. C. Yang, 2006), Figure 22 reveals that even if the same peak pore radius is considered, ignoring the effect of individual pore group will alter the ion concentration distribution. So, using the single peak radius is not enough to fully capture the influence of pore structure on concrete transport properties.

8 | CONCLUSION

From microstructure generation to chloride diffusivity prediction, a multi-scale chloride transport model, which links the chloride diffusion coefficient with the PSD, is proposed to analyze the pore size effect on chloride penetration directly. Based on the present model, the following conclusions can be drawn:

(1) Based on the hydration kinetic analysis, factors such as chemical compositions of cement clinkers, reaction temperature, and *w/c* ratio are considered to calculate the different hydration products' volume fractions. Using "porous growth" and "hard core-soft shell" methods, the complex microstructure of cement paste at different scales can be presented by 1000^3 voxel-based RVE. The new porous growth method can better reveal the irregular shapes and embedded pores within the microstructure. Based on the generated 3D multi-scale microstructures, irregular pore structures, including gel pores and small and LCPs, can be visually presented.

(2) Based on the voxel-based microstructure, the multi-modal PSDs covering a large range of pores can be extracted through Sub-model I, which shows agreement with the experimental data measured

by MIP tests. By applying different diffusivities to different voxels, the steady-state chloride diffusion process in generated multi-scale microstructures can be modeled. The chloride diffusivities of cement paste with different *w/c* and hydration degrees can then be predicted by Sub-model II.

(3) Compared with the model adopting single *D*, the chloride penetration depths predicted by the proposed framework, which considers multi-modal PSDs $p(r)$ and pore size-related diffusivities $D(r)$, are in better accordance with experimental data, with 10%–25% reduced prediction error.

(4) Even if the total porosity and averaged peak pore radius are the same, the altered PSD will greatly change the chloride transport process. Therefore, multi-modal pore sizes rather than single PSDs are necessary to be considered in concrete transport models.

The present work studies the chloride penetration in concrete, carefully considering the effect of widely ranged pore sizes from nano-gel pores to micro-capillary pores. However, future work still needs to address the following aspects. First, the generation procedures of three-dimensional microstructure with larger RVE sizes and finer resolutions should be further investigated. Second, micro-cracks may also occur in the microstructure leading to an increasing diffusivity, so the effect of cracks on chloride penetration should be taken into account. Third, microscopic modeling of chloride transport under humidity and temperature changes needs further study.

REFERENCES

Achour, M., Bignonnet, F., Barthélémy, J.-F., Rozière, E., & Amiri, O. (2020). Multi-scale modeling of the chloride diffusivity and the elasticity of Portland cement paste. *Construction and Building Materials*, *234*, 117124.

Adeli, H., & Kim, H. (2001). Cost optimization of composite floors using neural dynamics model. *Communications in Numerical Methods in Engineering*, *17*(11), 771–787.

Ahmadkhanlou, F., & Adeli, H. (2005). Optimum cost design of reinforced concrete slabs using neural dynamics model. *Engineering Applications of Artificial Intelligence*, *18*(1), 65–72.

Aldwaik, M., & Adeli, H. (2016). Cost optimization of reinforced concrete flat slabs of arbitrary configuration in irregular highrise building structures, *Structural and Multidisciplinary Optimization*, *54*(1), 151–164.

Bentz, D. P. (1997). Three-dimensional computer simulation of Portland cement hydration and microstructure development. *Journal of the American Ceramic Society*, *80*(1), 3–21.

Bentz, D. P., & Garboczi, E. J. (1991). Percolation of phases in a three-dimensional cement paste microstructural model. *Cement and Concrete Research*, *21*(2), 325–344.

Bernard, O., Ulm, F.-J., & Lemarchand, E. (2003). A multiscale micromechanics-hydration model for the early-age elastic properties of cement-based materials. *Cement and Concrete Research*, *33*(9), 1293–1309.

Bishnoi, S., & Scrivener, K. L. (2009). µic: A new platform for modelling the hydration of cements. *Cement and Concrete Research*, *39*(4), 266–274.

Blunt, M. J., Bijeljic, B., Dong, H., Gharbi, O., Iglauer, S., Mostaghimi, P., Paluszny, A., & Pentland, C. (2013). Pore-scale imaging and modelling. *Advances in Water Resources*, *51*, 197–216.

Cai, Y., Liu, Q.-F., Meng, Z., Chen, M., Li, W., & Šavija, B. (2022). Influence of coarse aggregate settlement induced by vibration on long-term chloride transport in concrete: A numerical study. *Materials and Structures*, *55*(9), 235.

Chen, D., Li, Y., Tao, J., Li, Y., Zhang, S., Shan, X., Wang, T., Qiao, Z., Zhao, R., Fan, X., & Zhou, Z. (2024). Deep learning-based segmentation model for permeable concrete meso-structures. *Computer-Aided Civil and Infrastructure Engineering*. Advance online publication. https://doi.org/10.1111/mice.13300

Chen, D., Yang, K., Hu, D., & Shi, J. (2021). A meso-stochastic research on the chloride transport in unsaturated concrete. *Construction and Building Materials*, *273*, 121986.

Chidiac, S. E., & Shafikhani, M. (2019). Phenomenological model for quantifying concrete chloride diffusion coefficient. *Construction and Building Materials*, *224*, 773–784.

Constantinides, G., & Ulm, F.-J. (2004). The effect of two types of C-S-H on the elasticity of cement-based materials: Results from nanoindentation and micromechanical modeling. *Cement and Concrete Research*, *34*(1), 67–80.

Constantinides, G., & Ulm, F.-J. (2007). The nanogranular nature of C–S–H. *Journal of the Mechanics and Physics of Solids*, *55*(1), 64–90.

Dridi, W. (2012). Analysis of effective diffusivity of cement based materials by multi-scale modelling. *Materials and Structures*, *46*(1-2), 313–326.

Freeman, B. L., Cleall, P. J., & Jefferson, A. D. (2019). An indicator-based problem reduction scheme for coupled reactive transport models. *International Journal for Numerical Methods in Engineering*, *120*(13), 1428–1455.

Gan, Y., Romero Rodriguez, C., Schlangen, E., van Breugel, K., & Šavija, B. (2021). Assessing strain rate sensitivity of cement paste at the micro-scale through micro-cantilever testing. *Cement and Concrete Composites*, *121*, 104084.

Gan, Y., Romero Rodriguez, C., Zhang, H., Schlangen, E., van Breugel, K., & Šavija, B. (2021). Modeling of microstructural effects on the creep of hardened cement paste using an experimentally informed lattice model. *Computer-Aided Civil and Infrastructure Engineering*, *36*(5), 560–576.

Guo, B., Hong, Y., Qiao, G., & Ou, J. (2018). A COMSOL-PHREEQC interface for modeling the multi-species transport of saturated cement-based materials. *Construction and Building Materials*, *187*, 839–853.

Guo, Y., Zhang, T., Du, J., Wang, C., Wei, J., & Yu, Q. (2021). Evaluating the chloride diffusion coefficient of cement mortars based on the tortuosity of pore structurally-designed cement pastes. *Microporous and Mesoporous Materials*, *317*, 111018.

Haecker, C. J., Garboczi, E. J., Bullard, J. W., Bohn, R. B., Sun, Z., Shah, S. P., & Voigt, T. (2005). Modeling the linear elastic properties of Portland cement paste. *Cement and Concrete Research*, *35*(10), 1948–1960.

Hafezolghorani, M., Hejazi, F., Jaffar, M. S., & Adeli, H. (2022). Plasticity model for partially prestressed concrete. *Structures*, *38*, 630–651.

Hu, X., Shi, C., Shi, Z., & Zhang, L. (2019). Compressive strength, pore structure and chloride transport properties of alkali-activated slag/fly ash mortars. *Cement and Concrete Composites*, *104*, 103392.

Huang, Q., Jiang, Z., Gu, X., Zhang, W., & Guo, B. (2015). Numerical simulation of moisture transport in concrete based on a pore size distribution model. *Cement and Concrete Research*, *67*, 31–43.

Jennings, H. M. (2000). A model for the microstructure of calcium silicate hydrate in cement paste. *Cement and Concrete Research*, *30*, 101–116.

Jia, D., Brigham, J. C., & Fascetti, A. (2024). An efficient static solver for the lattice discrete particle model. Computer-Aided Civil and Infrastructure Engineering. Advance online publication. https://doi.org/10.1111/mice.13306

Jin, C., Wang, S., Liu, P., Yang, X., & Oeser, M. (2023). Virtual modeling of asphalt mixture beam using density and distributional controls of aggregate contact. *Computer-Aided Civil and Infrastructure Engineering*, *38*(16), 2242–2256.

Kliukas, R., Daniunas, A., Gribniak, V., Lukoseviciene, O., Vanagas, E., & Patapavicius, A. (2018). Half a century of reinforced concrete electric poles maintenance: Inspection, field-testing, and performance assessment. *Structure and Infrastructure Engineering*, *14*(9), 1221–1232.

Li, L., Yang, J., Li, H., & Du, Y. (2022). Comparative study on backscattered electron image of cement paste quantified by frequency histogram, overflow and Gaussian distribution fitting method. *Journal of Materials in Civil Engineering*, *34*(7), 04022124.

Li, X., Huang, Y., Zhou, Y., Wang, X., Zhao, D., & Chen, C. (2024). Predicting the life cycle durability and ecological performance of cementitious coatings with a fuzzy-stochastics–based approach. *Computer-Aided Civil and Infrastructure Engineering*, *39*(7), 983–1002.

Liu, C., & Zhang, M. (2022). Multiscale modelling of ionic diffusivity in unsaturated concrete accounting for its hierarchical microstructure. *Cement and Concrete Research*, *156*, 106766.

Liu, L., Chen, H., Sun, W., & Ye, G. (2013). Microstructure-based modeling of the diffusivity of cement paste with micro-cracks. *Construction and Building Materials*, *38*, 1107–1116.

Liu, Q.-F. (2022). Progress and research challenges in concrete durability: Ionic transport, electrochemical rehabilitation and service life prediction. *RILEM Technical Letters*, *7*, 98–111.

Liu, Q.-F., Cai, Y., Peng, H., Meng, Z., Mundra, S., & Castel, A. (2023). A numerical study on chloride transport in alkali-activated fly ash/slag concretes. *Cement and Concrete Research*, *166*, 107094.

Liu, Q.-F., Hu, Z., Wang, X.-E., Zhao, H., Qian, K., Li, L.-J., & Meng, Z. (2022). Numerical study on cracking and its effect on chloride transport in concrete subjected to external load. *Construction and Building Materials*, *325*, 126797.

Liu, Z., Zhang, Y., Jiang, Q., Zhang, W., & Wu, J. (2014). Solid phases percolation and capillary pores depercolation in hydrating cement pastes. *Journal of Materials in Civil Engineering*, *26*(12), 04014090.

Lu, C., Danzer, R., & Fischer, F. D. (2002). Fracture statistics of brittle materials: Weibull or normal distribution. *Physical Review E*, *65*(6), 067102.

Luping, T., & Nilsson, L.-O. (1993a). Chloride binding capacity and binding isotherms of OPC pastes and mortars. *Cement and Concrete Research*, *23*(2), 247–253.

Luping, T., & Nilsson, L.-O. (1993b). Rapid determination of the chloride diffusivity in concrete by applying an electric field. *Materials*, *89*, 49–53.

Ma, H., Hou, D., Lu, Y., & Li, Z. (2014). Two-scale modeling of the capillary network in hydrated cement paste. *Construction and Building Materials*, *64*, 11–21.

Maekawa, K. (2008). *Multi-scale modeling of structural concrete*. CRC Press.

Maekawa, K., Ishida, T., & Kishi, T. (2003). Multi-scale modeling of concrete performance integrated material and structural mechanics. *Journal of Advanced Concrete Technology*, *1*(2), 91–126.

Martiń-Pérez, B., Zibara, H., Hooton, R. D., & Thomas, M. D. A. (2000). A study of the effect of chloride binding on service life predictions. *Cement and Concrete Research*, *30*(8), 1215–1223.

McDonald, P. J., Rodin, V., & Valori, A. (2010). Characterisation of intra- and inter-C–S–H gel pore water in white cement based on an analysis of NMR signal amplitudes as a function of water content. *Cement and Concrete Research*, *40*(12), 1656–1663.

Meng, Z., Liu, Q.-F., Ukrainczyk, N., Mu, S., Zhang, Y., & De Schutter, G. (2024). Numerical study on the chemical and electrochemical coupling mechanisms for concrete under combined chloride-sulfate attack. *Cement and Concrete Research*, *175*, 107368.

Meng, Z., Liu, Q.-F., Xia, J., Cai, Y., Zhu, X., Zhou, Y., & Pel, L. (2022). Mechanical–transport–chemical modeling of electrochemical repair methods for corrosion-induced cracking in marine concrete. *Computer-Aided Civil and Infrastructure Engineering*, *37*(14), 1854–1874.

Meng, Z., Zhang, Y., Chen, W.-K., Fu, C.-Q., Xiong, Q. X., Zhang, C.-L., & Liu, Q.-F. (2024). A numerical study of moisture and ionic transport in unsaturated concrete by considering multi-ions coupling effect. *Transport in Porous Media*, *151*(2), 339–366.

Ngala, V. T., Page, C. L., Parrott, L. J., & Yu, S. W. (1995). Diffusion in cementitious materials: II, further investigations of chloride and oxygen diffusion in well-cured OPC and OPC/30%PFA pastes. *Cement and Concrete Research*, *25*(4), 819–826.

Page, C. L., Short, N. R., & El Tarras, A. (1981). Diffusion of chloride ions in hardened cement pastes. *Cement and Concrete Research*, *11*(3), 395–406.

Patel, R. A., Churakov, S. V., & Prasianakis, N. I. (2021). A multi-level pore scale reactive transport model for the investigation of combined leaching and carbonation of cement paste. *Cement and Concrete Composites*, *115*, 103831.

Provis, J. L., Myers, R. J., White, C. E., Rose, V., & van Deventer, J. S. J. (2012). X-ray microtomography shows pore structure and tortuosity in alkali-activated binders. *Cement and Concrete Research*, *42*(6), 855–864.

Qiu, Q., & Dai, J.-G. (2021). Meso-scale modeling of chloride diffusivity in mortar subjected to corrosion-induced cracking. *Computer-Aided Civil and Infrastructure Engineering*, *36*(5), 602–619.

Raeini, A. Q., Bijeljic, B., & Blunt, M. J. (2017). Generalized network modeling: Network extraction as a coarse-scale discretization of the void space of porous media. *Physical Review E*, *96*(1-1), 013312.

Rafiei, M. H., Khushefati, W. H., Demirboga, R., & Adeli, H. (2016). Neural network, machine learning, and evolutionary approaches for concrete material characterization. *Materials*, *113*, 781–789.

Rafiei, M. H., Khushefati, W. H., Demirboga, R., & Adeli, H. (2017a). Novel approach for concrete mixture design using neural dynamics model and virtual lab concept. *ACI Materials Journal*, *114*, 117–127.

Rafiei, M. H., Khushefati, W. H., Demirboga, R., & Adeli, H. (2017b). Supervised deep restricted Boltzmann machine for estimation of concrete. *Materials*, *114*, 237–244.

Roy, D. M. (1988). Relationships between permeability, porosity, diffusion and microstructure of cement pastes, mortar, and concrete at different temperatures. *MRS Proceedings*, *137*, 179.

Sakai, Y. (2019). Relationship between pore structure and chloride diffusion in cementitious materials. *Construction and Building Materials*, *229*, 116868.

Scherer, G. W. (1999). Structure and properties of gels. *Cement and Concrete Research*, *29*(8), 1149–1157.

Shafikhani, M., & Chidiac, S. E. (2020). A holistic model for cement paste and concrete chloride diffusion coefficient. *Cement and Concrete Research*, *133*, 106049.

Shi, X., Fay, L., Yang, Z., Nguyen, T. A., & Liu, Y. (2009). Corrosion of deicers to metals in transportation infrastructure: Introduction and recent developments. *Corrosion Reviews*, *27*(1-2), 23–52.

Spiesz, P., & Brouwers, H. J. H. (2012). Influence of the applied voltage on the rapid chloride migration (RCM) test. *Cement and Concrete Research*, *42*(8), 1072–1082.

Tennis, P. D., & Jennings, H. M. (2000). A model for two types of calcium silicate hydrate in the microstructure of Portland cement pastes. *Cement and Concrete Research*, *30*(6), 855–863.

Thomas, J. J., Biernacki, J. J., Bullard, J. W., Bishnoi, S., Dolado, J. S., Scherer, G. W., & Luttge, A. (2011). Modeling and simulation of cement hydration kinetics and microstructure development. *Cement and Concrete Research*, *41*(12), 1257–1278.

Tong, L.-Y., Xiong, Q. X., Zhang, M., Meng, Z., Meftah, F., & Liu, Q.-F. (2023). Multi-scale modelling and statistical analysis of heterogeneous characteristics effect on chloride transport properties in concrete. *Construction and Building Materials*, *367*, 130096.

Tong, L.-Y., Zhao, J., & Cheng, Z. (2021). Chloride ion binding effect and corrosion resistance of geopolymer materials prepared with seawater and coral sand. *Construction and Building Materials*, *309*, 125126.

Venkovic, N., Sorelli, L., Sudret, B., Yalamas, T., & Gagné, R. (2013). Uncertainty propagation of a multiscale poromechanics-hydration model for poroelastic properties of cement paste at early-age. *Probabilistic Engineering Mechanics*, *32*, 5–20.

Wan, T., Wang, H., Yang, X., Chen, Y., Li, L., & Diab, A. (2024). Thermal contraction coordination behavior between unbound aggregate layer and asphalt mixture overlay based on the finite difference and discrete element coupling method. *Computer-Aided Civil and Infrastructure Engineering*, *39*(14), 2140–2158.

Xiong, Q. X., & Meftah, F. (2021). Determination on pore size distribution by a probabilistic porous network subjected to salt precipitation and dissolution. *Computational Materials Science*, *195*, 110491.

Xiong, Q. X., Tong, L.-Y., Meftah, F., Zhang, Y., & Liu, Q.-F. (2024). Improved predictions of permeability properties in cement-based materials: A comparative study of pore size distribution-based models. *Construction and Building Materials*, *411*, 133927.

Xiong, Q. X., Tong, L.-Y., Zhang, Z., Shi, C., & Liu, Q.-F. (2023). A new analytical method to predict permeability properties of cementitious mortars: The impacts of pore structure evolutions and relative humidity variations. *Cement and Concrete Composites*, *137*, 104912.

Yang, C. C. (2006). On the relationship between pore structure and chloride diffusivity from accelerated chloride migration test in cement-based materials. *Cement and Concrete Research*, *36*(7), 1304–1311.

Yang, S., Ukrainczyk, N., Caggiano, A., & Koenders, E. (2021). Numerical phase-field model validation for dissolution of minerals. *Applied Sciences (Switzerland)*, *11*(6), 2464.

Ye, G., van Breugel, K., & Fraaij, A. L. A. (2003). Three-dimensional microstructure analysis of numerically simulated cementitious materials. *Cement and Concrete Research*, *33*(2), 215–222.

Yu, S. W., & Page, C. L. (1991). Diffusion in cementitious materials: 1. Comparative study of chloride and oxygen diffusion in hydrated cement pastes. *Cement and Concrete Research*, *21*(4), 581–588.

Zhang, M., Ye, G., & van Breugel, K. (2012). Modeling of ionic diffusivity in non-saturated cement-based materials using lattice Boltzmann method. *Cement and Concrete Research*, *42*(11), 1524–1533.

Zhang, Y., Yang, Z., & Ye, G. (2020). Dependence of unsaturated chloride diffusion on the pore structure in cementitious materials. *Cement and Concrete Research*, *127*, 105919.

Zhang, Y., & Ye, G. (2019). A model for predicting the relative chloride diffusion coefficient in unsaturated cementitious materials. *Cement and Concrete Research*, *115*, 133–144.

Zheng, J., Zhang, J., Zhou, X., & Wang, X. (2019). Numerical method for predicting chloride diffusivity of mature cement paste. *Journal of Materials in Civil Engineering*, *31*(6), 04019080.

How to cite this article: Tong, L.-Y., Liu, Q.-F., Xiong, Q., Meng, Z., Amiri, Q., & Zhang, M. (2024). Modeling the chloride transport in concrete from microstructure generation to chloride diffusivity prediction. *Computer-Aided Civil and Infrastructure Engineering*, 1–21. https://doi.org/10.1111/mice.13331